

1

Casimir Forces and Geometry in Nanosystems*Thorsten Emig¹⁾*

Casimir interactions, predicted in 1948 [15, 14] between atoms and macroscopic surfaces, and probed in a series of high precision experiments over the past decade [46, 50, 8], are particularly important at micro-meter to nano-meter length scales due to their strong power-law increase at short separations between particles. Therefore, in constructing and operating devices at these length scales it is important to have an accurate understanding of material, shape and geometry dependence of these forces. In particular, the observation of Casimir forces in devices on sub-micron scales has generated great current interest in exploring the role of these forces for the development and optimization of micro- and nano-electromechanical systems [9, 17, 16]. These systems can serve as on-chip fully integrated sensors and actuators with a growing number of applications. It was pointed out that Casimir forces can make an important contribution to the principal cause of malfunctions of these devices in form of stiction that results in permanent adhesion of nearby surface elements [10]. This initiated interest in repulsive Casimir forces by modifying material properties as well as the geometry of the interacting components [11, 43, 52].

The study of fluctuation induced forces has a long history. When these forces result from fluctuations of charges and currents inside particles or macroscopic objects, they are usually summarized under the general term van der Waals forces [55]. This interaction appears at the atomic scale in the guise of Keesom, Debye, London, and Casimir-Polder forces. An important property of all these interactions is their non-additivity: The total interaction of macroscopic objects is in general not given by the sum of the interactions between all pairs of particles that form the objects. This inherent many-body character of the force leads to interesting and often unexpected behavior but renders the study of these forces also a difficult problem. Commonly used approximations as pairwise additivity assumptions become unreliable for systems of condensed atoms. The collective interaction of condensed macroscopic systems is better formulated in terms of their dielectric properties. Such a formulation was es-

¹⁾Institut für Theoretische Physik, Universität zu Köln, Zùlpicher Strasse 77, 50937 Köln, Germany; Laboratoire de Physique Théorique et Modèles Statistiques, CNRS UMR 8626, Bât. 100, Université Paris-Sud, 91405 Orsay cedex, France

established by Lifshitz for two parallel and planar, infinitely extended dielectric surfaces [47], extending Casimir's original work for perfect metals. In practice, one encounters objects of finite size with curved surfaces and/or edges, like structured surfaces, spheres or cylinders. Also, in small-scale devices often more than two objects are at close separation and one would like to know the collective effects resulting from non-additivity. In this chapter we shall encounter a selection of examples for interesting behavior of fluctuation forces that result from shape and material properties that have been obtained from a recently developed method that makes it possible to compute van der Waals-Casimir interactions for arbitrary compact objects based on their scattering properties for electromagnetic waves [32, 33, 30, 42].

1.1

Casimir effect

The Casimir effect is the attraction between two uncharged, parallel and perfectly conducting plates [14]. For this simple geometry the interaction can be obtained directly from the plate induced *change* of the energies of the quantum mechanical harmonics oscillators associated with the normal modes of the electromagnetic field. The derivation given here follows closely the one originally presented by Casimir. Consider two parallel and planar surfaces of size $L \times L$ and separation d . We assume that the system is at zero temperature so that the interaction is given by the ground state energies of harmonic oscillators. When we are interested in the pressure (force per plate area L^2) between large plates with $L \gg d$, we can ignore edge effects $\sim L$ and allow for a continuum of wave vectors parallel to the plates. For a perfect conductor the tangential electric field has to vanish at the surface and the normal modes correspond to the allowed wave vectors $\mathbf{k} = (\mathbf{k}_{\parallel}, \pi n/d)$ where \mathbf{k}_{\parallel} is the two-dimensional wave vector parallel to the plates. The linear dispersion of photons yields the eigenfrequencies $\omega_{n\mathbf{k}_{\parallel}} = c\sqrt{k_{\parallel}^2 + (\pi n/d)^2}$ so that the ground state energy becomes

$$E = \frac{\hbar}{2} \sum'_{n=0} \left(\frac{L}{2\pi} \right)^2 \int d^2 k_{\parallel} 2\omega_{n\mathbf{k}_{\parallel}}, \quad (1.1)$$

where we have included a factor of 2 since for each mode with $n \neq 0$ exist two polarizations. The primed summation assigns a weight of 1/2 to the term for $n = 0$. Obviously, the expression of Eq. (1.1) is divergent. This is a consequence of the assumption that the surfaces behave as a perfect conductor for arbitrarily high frequencies. In practice, as pointed out by Casimir, for very high frequencies (X-rays, e.g.) the plates are hardly an obstacle for electromagnetic waves and therefore the ground state energy of these modes will not be changed by the presence of the plates. We implement this observation by introducing a cut-off function $\chi(z)$ that is regular at $z = 0$ with $\chi(0) = 1$ and vanishes, along with all its derivatives, for $z \rightarrow \infty$ sufficiently fast. After a change of variables, $\omega = c\sqrt{k_{\parallel}^2 + (\pi n/d)^2}$ with $c^2 k_{\parallel} dk_{\parallel} = \omega d\omega$, we

obtain the finite expression for the energy

$$E = \frac{\hbar L^2}{2\pi c^2} \sum_{n=0}^{\infty} f(n) \quad \text{with} \quad f(n) = \int_{\pi n c/d}^{\infty} \omega^2 \chi(\omega/\omega_c) d\omega \quad (1.2)$$

where ω_c is a cut-off frequency. As mentioned before, we are interested in the change of the energy due the presence of the plates. Let us imagine that we increase the separation d between the plates to infinity, thus creating empty space. When we subtract the energy of the latter configuration from the total energy of Eq. (1.2), we obtain the change in energy that is the relevant interaction potential between the plates. When the separation d tends to infinity, the sum in Eq. (1.2) can be replaced by an integral, yielding after the substitution $\Omega = \pi n c/d$ the energy

$$E_{\infty} = \frac{\hbar}{2\pi^2 c^3} L^2 d \int_0^{\infty} d\Omega \tilde{f}(\Omega) \quad \text{with} \quad \tilde{f}(\Omega) = \int_{\Omega}^{\infty} \omega^2 \chi(\omega/\omega_c) d\omega. \quad (1.3)$$

As expected, the energy E_{∞} is proportional to the volume $L^2 d$ of empty space and to a cut-off dependent factor that is given by the integrals of Eq. (1.3). This factor describes the self-energy of the bounding surfaces. It is infinite for perfect conductors which correspond to $\omega_c \rightarrow \infty$. For a non-ideal conductor or any other material this factor is finite but depends on material properties like the plasma wavelength for a metal. Now we compute the change in energy when the plates are moved in from infinity,

$$\Delta E = E - E_{\infty} = \frac{\hbar L^2}{2\pi c^2} \left[\sum_{n=0}^{\infty} f(n) - \int_0^{\infty} dn f(n) \right]. \quad (1.4)$$

The difference between the sum and the integral is given by the Euler-Maclaurin formula $\sum_{n=0}^{\infty} f(n) - \int_0^{\infty} dn f(n) = -\frac{1}{12} f'(0) + \frac{1}{6!} f'''(0) + \mathcal{O}(f^{(5)}(0))$. This series of derivatives of odd order can be truncated in the limit of perfect conductors $\omega_c \rightarrow \infty$ since $f'(0) = 0$, $f'''(0) = -2(\pi c/d)^3$ and $f^{(\nu)}(0) \sim (c/d)^3 (c/d\omega_c)^{\nu-3}$. The Casimir potential hence becomes

$$\Delta E = -\frac{\pi^2}{720} \frac{\hbar c}{d^3} L^2 + \mathcal{O}(\omega_c^{-2}), \quad (1.5)$$

and the pressure for perfect metal plates is

$$\frac{F}{L^2} = -\frac{\pi^2}{240} \frac{\hbar c}{d^4}. \quad (1.6)$$

The interesting fact is that the amplitude of the interaction is *universal*, i.e., independent of the cut-off that can be viewed as a simplified description of a real metal. This implies that for any pair of surfaces with metallic response in the limit of small frequencies $\omega \rightarrow 0$ the interaction at asymptotically large separations is described by the potential of Eq. (1.5). At a separation of $d = 100\text{nm}$ Eq. (1.6) yields a pressure of $1.28 \cdot 10^{-4}$ atm or 13.00 Pa.

1.2

Dependence on Shape and Geometry

Casimir interactions result from a modification of the fluctuation spectrum of the electromagnetic field due to boundaries or coupling to matter. This suggests that these interactions strongly depend on the shape of the interacting objects and geometry, i.e., relative position and orientation. The most commonly encountered geometry is a sphere-plate setup that was used in the first high-precision tests of the Casimir effect [46, 50]. This geometry has been successfully used ever since in most of the experimental studies of Casimir forces between metallic surfaces [60, 27, 17, 21, 19, 25, 20, 51]. In order to keep the deviations from two parallel plates sufficiently small, a sphere with a radius much larger than the surface distance has been used. The effect of curvature has been accounted for by the “proximity force approximation” (PFA) [55]. This scheme is assumed to describe the interaction for sufficiently small ratios of radius of curvature to distance. However, this uncontrolled assumption since PFA becomes exact only for infinitesimal separations, and corrections to PFA are generally unknown.

At the other extreme, the interaction between a planar surface and an object that is either very small or at an asymptotically large distance is governed by the Casimir-Polder potential that was derived for the case of an atom and a perfectly conducting plane [15]. There have been attempts to go beyond the two extreme limits of asymptotically large and small separations by measuring the Casimir force between a sphere and a plane over a larger range of ratios of sphere radius to distance [44].

Until very recently, no practical tools were available to compute the electromagnetic Casimir interaction between objects of arbitrary shape at all distances, including the important sphere-plate geometry. Progress in understanding the geometry dependence of fluctuation forces was hampered by the lack of methods that are applicable over a wide range of separations. Unlike the case of parallel plates, the eigenvalues of the Helmholtz equation in more complicated geometries are in general not known and a summation over normal modes, as in the original Casimir calculation of Section 1.1, is not practical. Conceptually, the effects of geometry and shape are difficult to study due to the non-additivity of fluctuation forces.

For some decades, there has been considerable interest in the theory of Casimir forces between objects with curved surfaces. Two types of approaches have been pursued. Attempts to compute the force explicitly in particular geometries and efforts to develop a general framework which yields the interaction in terms of characteristics of the objects like polarizability or curvature. Within the second type of approach, Balian and Duplantier studied the electromagnetic Casimir interaction between compact and perfect metallic shapes in terms of a multiple reflection expansion and derived also explicit results to leading order at asymptotically large separations [4, 5]. For parallel and partially transmitting plates a connection to scattering theory has been established which yields the Casimir interaction of the plates as a determinant of a diagonal matrix of reflection amplitudes [40]. For non-planar, deformed plates, a general representation of the Casimir energy as a functional determinant of a matrix that describes reflections at the surfaces and free propagation between them has been developed in Ref. [31].

Later on, an equivalent representation has been applied to perturbative computations in the case of rough and corrugated plates with finite conductivity [45, 54, 53].

Functional determinant formulas have been used also for open geometries that do not fall into the class of parallel plates with deformations. For the Casimir interaction between planar plates and cylinders, a partial wave expansion of the functional determinant has been employed [36, 6]. More recently, a new method based on a multipole expansion of fluctuating currents inside the objects has been developed [32, 33, 30]. This method allows for accurate and efficient calculations of Casimir forces and torques between compact objects of arbitrary shape and material composition in terms of the scattering matrices of the *individual* objects. A similar scattering approach has been developed in Ref. [42].

In this Section three examples for the strong geometry dependence of Casimir forces will be made explicit. First, an overview on forces between *deformed and structured surfaces* will be given. The interactions are obtained from both a perturbative and numerical evaluation of a functional determinant representation of Casimir interactions between ideal metal surfaces. As a second example we describe the effects that occur in the interaction of *one-dimensional structures as cylinders and wires* and related non-additivity phenomena for more than two objects. Finally, as an example for the interaction between compact objects, the Casimir force between *metallic spheres* is presented for the full range of separations, covering the crossover from the asymptotic Casimir-Polder law to proximity approximations. The analysis of the last two examples is based on a scattering approach.

1.2.1

Deformed surfaces

The dependence of the Casimir force on shape and material properties offers the opportunity to manipulate this interaction in a controlled way, e.g., by imprinting patterns on the interacting surfaces. It has been shown that a promising route to this end is via modifications of the parallel plate geometry [38, 34, 35]. The corrections due to deformations, such as sinusoidal corrugations, of the metal plates can be significant. In searching for non-trivial shape dependences, Roy and Mohideen [61] measured the force between a sphere with large radius and a sinusoidally corrugated plate with amplitude $a \approx 60\text{nm}$ and wavelength $\lambda \approx 1.1\mu\text{m}$. Over the range of separations $H \approx 0.1 - 0.9\mu\text{m}$, the observed force showed clear deviations from the dependence expected on the basis of decomposing the Casimir force to a sum of pairwise contributions (in effect, an average over the variations in separations). Motivated by this experiment, the effect of corrugations on the Casimir force between surfaces has been studied without using pairwise additivity approximations. The analysis is based on a path integral quantization of the fluctuating field with appropriate boundary conditions which leads to a functional determinant representation of the Casimir energy [38] which can be evaluated perturbatively for a small deformation amplitude [34, 35] or numerically for general amplitudes [28, 12, 13]. In recent experiments [18] the Casimir force between a gold sphere and a silicon surface with an array of nanoscale, rectangular corrugations

has been measured and the results were found to be consistent with the theory based on a numerical evaluation of functional determinants for ideal metals (see below). Qualitative agreement can be expected only when material properties are taken into account in addition to shape.

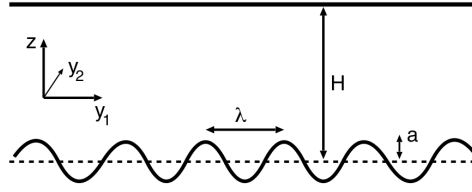


Fig. 1.1 Configuration of a flat and a corrugated plate at mean separation H .

While we will be interested in the interaction between flat and corrugated surfaces as depicted in Figs. 1.1, 1.4, first of all we consider two surfaces with arbitrary *uniaxial* deformations without overhangs so that their profiles can be described by height functions $h_\alpha(y_1)$ ($\alpha = 1, 2$ for the two surfaces), with $\int dy_1 h_\alpha(y_1) = 0$. It is further assumed that the surfaces are perfectly conducting and infinitely extended along the plane spanned by $\mathbf{y}_\parallel = (y_1, y_2)$. As explained before for two planar plates, the Casimir energy at zero temperature corresponds to the difference of the ground state energies of the quantized electromagnetic field for plates at distance H and at $H \rightarrow \infty$, respectively. To obtain this energy, we employ a path integral quantization method. For general, non-uniaxial deformations or objects of more general shape, it is necessary to consider the action for the electromagnetic field since the two polarizations (TM for transverse magnetic waves and TE for transverse electric waves) are coupled. However, for the uniaxial deformations under consideration here, we can develop a simpler quantization scheme, by a similar reasoning as used in the context of waveguides with constant cross-sectional shape [34]. In this case, the two polarizations are *independent* modes which do not couple under scattering between the surfaces. For TM waves all field components are then fully specified by a scalar field corresponding to the electric field along the invariant direction,

$$\Phi_{\text{TM}}(t, y_1, y_2, z) = E_2(t, y_1, y_2, z), \quad (1.7)$$

with the Dirichlet boundary condition $\Phi_{\text{TM}}|_{S_\alpha} = 0$ on each surface S_α . The TE waves are analogously described by the scalar field

$$\Phi_{\text{TE}}(t, y_1, y_2, z) = B_2(t, y_1, y_2, z), \quad (1.8)$$

with the Neumann boundary condition $\partial_n \Phi_{\text{TE}}|_{S_\alpha} = 0$, where ∂_n is the normal derivative of the surface S_α pointing into the space between the two plates. After a Wick rotation to the imaginary time variable $X^0 = ict$, both fields Φ_{TM} and Φ_{TE} can be quantized using the Euclidean action

$$S\{\Phi\} = \frac{1}{2} \int d^4 X (\nabla\Phi)^2. \quad (1.9)$$

In order to obtain the change in the ground state energy that is associated with the presence of the plates, we now consider the partition functions \mathcal{Z}_D and \mathcal{Z}_N for the scalar field Euclidean action both with Dirichlet (D) and Neumann (N) boundary conditions at the surfaces. We implement the boundary conditions on the surfaces S_α using delta functions, which leads to the partition functions

$$\mathcal{Z}_D = \frac{1}{\mathcal{Z}_0} \int \mathcal{D}\Phi \prod_{\alpha=1}^2 \prod_{X_\alpha} \delta[\Phi(X_\alpha)] \exp(-S\{\Phi\}/\hbar), \quad (1.10)$$

$$\mathcal{Z}_N = \frac{1}{\mathcal{Z}_0} \int \mathcal{D}\Phi \prod_{\alpha=1}^2 \prod_{X_\alpha} \delta[\partial_n \Phi(X_\alpha)] \exp(-S\{\Phi\}/\hbar), \quad (1.11)$$

where \mathcal{Z}_0 is the partition function of the space without plates. Here $X_1(\mathbf{y}) = [\mathbf{y}, h_1(y_1)]$ and $X_2(\mathbf{y}) = [\mathbf{y}, H + h_2(y_1)]$, where $\mathbf{y} = (y_0, y_1, y_2) = (y_0, \mathbf{y}_\parallel)$, and $y_0 = ict$, is a parametrization of the plates in 4D Euclidean space. The Casimir energy \mathcal{E} per unit area (at zero temperature) that results from moving the plates in from infinity is obtained from the partition function as

$$\mathcal{E}(H) = E(H) - \lim_{H \rightarrow \infty} E(H), \quad (1.12)$$

with

$$E(H) = -\frac{\hbar c}{AL} [\ln \mathcal{Z}_D + \ln \mathcal{Z}_N], \quad (1.13)$$

where A is the surface area of the plates and the limit where the overall Euclidean length in time direction, L , tends to infinity is implicitly assumed. The partition functions can be expressed as functional determinants, using auxiliary fields (for details see Ref.[35]),

$$\ln \mathcal{Z}_D = -\frac{1}{2} \ln \det \mathbb{M}_D, \quad \ln \mathcal{Z}_N = -\frac{1}{2} \ln \det \mathbb{M}_N. \quad (1.14)$$

The kernels \mathbb{M}_D and \mathbb{M}_N are given by

$$[\mathbb{M}_D]_{\alpha\beta}(\mathbf{y}, \mathbf{y}') = [g_\alpha(y_1)]^{1/4} G[X_\alpha(\mathbf{y}) - X_\beta(\mathbf{y}')] [g_\beta(y'_1)]^{1/4}, \quad (1.15)$$

$$[\mathbb{M}_N]_{\alpha\beta}(\mathbf{y}, \mathbf{y}') = [g_\alpha(y_1)]^{1/4} \partial_{n_\alpha(y_1)} \partial_{n_\beta(y'_1)} G[X_\alpha(\mathbf{y}) - X_\beta(\mathbf{y}')] \times [g_\beta(y'_1)]^{1/4}, \quad (1.16)$$

where $g_\alpha(y_1) = 1 + [h'_\alpha(y_1)]^2$ is the determinant of the induced metric, and $n_\alpha(y_1) = (-1)^\alpha g_\alpha^{-1/2}(y_1) [h'_\alpha(y_1), 0, -1]$ is the normal vector to the surface S_α , while

$$G(\mathbf{x}) = \frac{1}{4\pi^2} \frac{1}{\mathbf{x}^2} \quad (1.17)$$

is the *free* Euclidean space Green's function with $\mathbf{x} = (\mathbf{y}, z)$. Eqs. (1.12) to (1.17) constitute the functional determinant representation of the Casimir interaction. This representation is exact. To proceed, the determinant has to be evaluated either by perturbation theory in the deformation amplitude or numerically for a specific shape of the surface profiles. First, we present the perturbative approach.

For both boundary conditions ($X = D, N$) we divide by the partition function $\mathcal{Z}_{X,\infty}$ for $H \rightarrow \infty$ and expand $\ln(\mathcal{Z}_X/\mathcal{Z}_{X,\infty})$ in a series $\ln(\mathcal{Z}_X/\mathcal{Z}_{X,\infty})|_0 + \ln(\mathcal{Z}_X/\mathcal{Z}_{X,\infty})|_1 + \ln(\mathcal{Z}_X/\mathcal{Z}_{X,\infty})|_2 + \dots$, where the subscript indicates the corresponding order in h_α . The lowest order result is

$$\ln(\mathcal{Z}_X/\mathcal{Z}_{X,\infty})|_0 = \frac{AL}{H^3} \frac{\pi^2}{1440} \quad (1.18)$$

for both types of modes, corresponding to two flat plates, cf. Eq. (1.5). The first order result $\ln(\mathcal{Z}_X/\mathcal{Z}_{X,\infty})|_1$ vanishes since we assume, without loss of generality, that the mean deformations are zero, $\int dy_1 h_\alpha(y_1) = 0$. The second order contribution is given by

$$\begin{aligned} \ln(\mathcal{Z}_X/\mathcal{Z}_{X,\infty})|_2 &= \frac{\pi^2}{240} \frac{1}{H^5} \int d^3y \{ [h_1(y_1)]^2 + [h_2(y_1)]^2 \} \\ &\quad - \frac{1}{2} \int d^3y \int d^3y' K_X(\mathbf{y} - \mathbf{y}') \left\{ \frac{1}{2} [h_1(y_1) - h_1(y'_1)]^2 + \frac{1}{2} [h_2(y_1) - h_2(y'_1)]^2 \right\} \\ &\quad - \frac{1}{2} \int d^3y \int d^3y' Q_X(\mathbf{y} - \mathbf{y}') [h_1(y_1)h_2(y'_1) + h_2(y_1)h_1(y'_1)]. \end{aligned} \quad (1.19)$$

The terms in the first row are local contributions which are identical for TM and TE modes. They follow also from a pairwise summation approximation (PWS) that sums a “renormalized” Casimir-Polder potential over the volumes of the interacting bodies [35]. The remaining terms are non-local and cannot be obtained in approximative schemes. For Dirichlet boundary conditions, the kernels depend only on $|\mathbf{y} - \mathbf{y}'|$ and are given by

$$K_D(y) = -\frac{1}{2\pi^4 y^8} + \frac{\pi^2}{128} \frac{1}{H^6 y^2} \frac{\cosh^2(s)}{\sinh^6(s)}, \quad (1.20)$$

$$Q_D(y) = \frac{\pi^2}{128} \frac{1}{H^6 y^2} \frac{\sinh^2(s)}{\cosh^6(s)}, \quad (1.21)$$

where $s = \pi y/(2H)$. The kernels for Neumann boundary conditions assume a more complicated form since the normal derivative breaks the equivalence of space and time directions. Hence, they depend separately on $|y_0 - y'_0|$ and $|\mathbf{y}_\parallel - \mathbf{y}'_\parallel|$. Their explicit form can be found in [35]. The results obtained so far apply to general uniaxial deformations of both surfaces.

Now we apply these results to the important case of corrugated plates. We begin with the geometry depicted in Fig. 1.1 which is parametrized by

$$h_1(y_1) = a \cos(2\pi y_1/\lambda), \quad \text{and} \quad h_2(y_1) = 0. \quad (1.22)$$

For this profile, the computation of the partition function to second order in a reduces to the Fourier transforming of the kernels with respect to y_1 . The corresponding expression for \mathcal{E} in Eq. (1.12) can be written as

$$\mathcal{E} = \mathcal{E}_0 + \mathcal{E}_{\text{cf}}, \quad (1.23)$$

where \mathcal{E}_0 is the energy per unit area of two flat plates [see Eq. (1.5)] and

$$\mathcal{E}_{\text{cf}} = -\frac{\hbar c a^2}{H^5} \left[G_{\text{TM}} \left(\frac{H}{\lambda} \right) + G_{\text{TE}} \left(\frac{H}{\lambda} \right) \right] + \mathcal{O}(a^3), \quad (1.24)$$

where the index cf of \mathcal{E}_{cf} stands for corrugated-flat geometry. The functions that describe the λ -dependence in this expression can be computed exactly [35]. They can be expressed in terms of the polylogarithm function $\text{Li}_n(z) = \sum_{\nu=1}^{\infty} z^\nu / \nu^n$, leading to

$$G_{\text{TM}}(x) = \frac{\pi^3 x}{480} - \frac{\pi^2 x^4}{30} \ln(1-u) + \frac{\pi}{1920x} \text{Li}_2(1-u) + \frac{\pi x^3}{24} \text{Li}_2(u) + \frac{x^2}{24} \text{Li}_3(u) + \frac{x}{32\pi} \text{Li}_4(u) + \frac{1}{64\pi^2} \text{Li}_5(u) + \frac{1}{256\pi^3 x} \left(\text{Li}_6(u) - \frac{\pi^6}{945} \right), \quad (1.25)$$

$$G_{\text{TE}}(x) = \frac{\pi^3 x}{1440} - \frac{\pi^2 x^4}{30} \ln(1-u) + \frac{\pi}{1920x} \text{Li}_2(1-u) - \frac{\pi x}{48} (1+2x^2) \text{Li}_2(u) + \left(\frac{x^2}{48} - \frac{1}{64} \right) \text{Li}_3(u) + \frac{5x}{64\pi} \text{Li}_4(u) + \frac{7}{128\pi^2} \text{Li}_5(u) + \frac{1}{256\pi^3 x} \left(\frac{7}{2} \text{Li}_6(u) - \pi^2 \text{Li}_4(u) + \frac{\pi^6}{135} \right) \quad (1.26)$$

with $u \equiv \exp(-4\pi x)$. Figure 1.2 displays separately the contributions from G_{TM} and G_{TE} to the corrugation induced correction \mathcal{E}_{cf} to the Casimir energy. While $G_{\text{TM}}(H/\lambda)$ is a monotonically increasing function of H/λ , $G_{\text{TE}}(H/\lambda)$ displays a minimum for $H/\lambda \approx 0.3$.

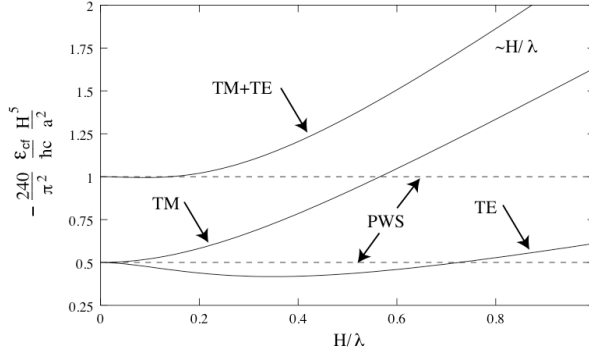


Fig. 1.2 Rescaled correction \mathcal{E}_{cf} to the Casimir energy due to the corrugation as given by Eq. (1.24) (upper curve). The lower curves show the separate contributions from TM and TE modes. The rescaling of \mathcal{E}_{cf} is chosen such that the corresponding prediction of the pairwise summation (PWS) approximation [corresponding to the local terms of Eq. (1.19)] is a constant (dashed lines).

Examining the limiting behaviors of Eq. (1.24) is instructive. In the limit $\lambda \gg H$, the functions G_{TM} and G_{TE} approach constant values, and the total Casimir energy takes the λ -independent form

$$\mathcal{E} = -\frac{\hbar c}{H^3} \frac{\pi^2}{720} \left(1 + 3 \frac{a^2}{H^2} \right) + \mathcal{O}(a^3). \quad (1.27)$$

Note that *only* in this case both wave types provide the same contribution to the total energy and the result agrees with the pairwise summation approximation (see Fig. 1.2). In the opposite limit of $\lambda \ll H$ both G_{TM} and G_{TE} grow linearly in H/λ . Therefore, in this limit the correction to the Casimir energy decays according to a *slower* power law in H , as

$$\mathcal{E} = -\frac{\hbar c}{H^3} \frac{\pi^2}{720} \left(1 + 2\pi \frac{a^2}{\lambda H}\right) + \mathcal{O}(a^3), \quad (1.28)$$

with an amplitude proportional to $1/\lambda$. Note that this behavior is completely missed by the pairwise summation approach which always yields a λ independent Casimir energy in the presence of modulations on one plate [35]. As we will discuss below in the context of the numerical approach, the apparent divergence for $\lambda \rightarrow 0$ in Eq. (1.28) is an artifact of the perturbative expansion which assumes that the amplitude a is the smallest length scale.

Next we turn to a numerical approach for computing the functional determinants of Eq. (1.14). Such an approach has been developed for periodic surface profiles in [28, 12]. In this approach, it is convenient to compute directly the Casimir force $F = -\partial_H \mathcal{E}$ per unit area which is the sum of TM and TE contributions, $F = F_{\text{TM}} + F_{\text{TE}}$ that according to Eq. (1.14) are given by (for $X = D, N$)

$$F_X = -\frac{\hbar c}{2AL} \text{Tr} (\mathbb{M}_X^{-1} \partial_H \mathbb{M}_X). \quad (1.29)$$

The right hand side of this expression is always finite, and no divergences due to self-energies have to be subtracted. The trace in Eq. (1.29) can be computed efficiently by Fourier transforming \mathbb{M} with respect to \mathbf{y}, \mathbf{y}' . The so transformed operator can then be transformed to block-diagonal form by making use of the periodicity of the surface profile along the y_1 direction. In this representation the blocks can be numbered by the wave vector $q_1 \in [0, 2\pi/\lambda)$ along the y_1 direction. A block matrix with label q_1 couples only waves whose momenta differ from the Bloch momentum q_1 by integer multiples of $2\pi/\lambda$. The integers multiplying $2\pi/\lambda$ number the matrix elements within a block matrix. Hence, the problem of computing the total trace has been simplified to the computation of the trace of each block matrix with label q_1 . Finally, integration over q_1 from 0 to $2\pi/\lambda$ and over the unrestricted momenta q_0, q_2 (along the time direction and invariant spatial direction of the surfaces, respectively) yields the force of Eq. (1.29). For the particular choice of a *rectangular* corrugation [see Fig. 1.5(a)] analytic expressions for all matrix elements of \mathbb{M} can be obtained. For details of the implementation of the numerical approach and expressions for the matrix elements see [12].

In analogy to the profile of Fig. 1.1 we consider the corresponding situation of a flat plate and a plate with a rectangular corrugation profile parametrized by

$$h_1(y_1) = \begin{cases} +a & \text{for } |y_1| < \lambda/4 \\ -a & \text{for } \lambda/4 < |y_1| < \lambda/2 \end{cases}, \quad (1.30)$$

and continuation by periodicity $h_1(y_1) = h_1(y_1 + n\lambda)$ for any integer n . The numerical results for the total Casimir force between the two plates is shown in Fig. 1.3 for different corrugation wavelengths λ . For all λ , the forces at a fixed separation H are bounded

between a minimal force F_∞ and a maximal force F_0 . For small λ/a the upper bound F_0 is approached whereas for asymptotically large λ/a the force converges towards the lower bound F_∞ . Analytic expressions can be derived for these bounds. For large λ , the corrugated surface is composed of large flat segments with a low density of edges. At sufficiently small surface separations $H \ll \lambda$ the main contribution to the force comes from wavelengths which are much smaller than the scale λ of the surface structure. Thus in the dominant range of modes diffraction can be neglected, and a simple proximity force approximation [55] should be applicable. Such an approximation assumes that the total force can be calculated as the sum of local forces between opposite *flat* and *parallel* small surface elements at their local distance $H - h_1(y_1)$. No distinction is made between TM and TE modes. This procedure is rather simple for the rectangular corrugation considered here since the surface has no curvature (except for edges). There are only two different distances $H + a$, $H - a$ which contribute one half each across the entire surface area, leading for $\lambda \rightarrow \infty$ to the proximity approximation for the force,

$$F_\infty/A = -\frac{\pi^2 \hbar c}{240} \frac{1}{2} \left[\frac{1}{(H-a)^4} + \frac{1}{(H+a)^4} \right]. \quad (1.31)$$

In the limit $\lambda \rightarrow 0$ the important fluctuations should not get into the narrow valleys of the corrugated plate. Even for small but finite λ this picture should be a good, though approximate, description since it still effects the wavelengths of order H which give the main contribution to the force. Thus one can expect that the plates feel a force which is equal to the force between two *flat* plates at the *reduced* distance $H - a$. Fortunately, this expectation can be checked by an explicit calculation since the leading part of determinant of \mathbb{M}_X in the limit $\lambda \rightarrow 0$ can be computed. Indeed, this computation confirms the expectation, leading to the Casimir force per surface area [12]

$$F_0/A = -\frac{\pi^2}{240} \frac{1}{(H-|a|)^4} \quad (1.32)$$

with equal contributions from TM and TE modes. Notice that this result is not analytic in a/H and is *exact* in the limit $\lambda \rightarrow 0$. As we have seen before, perturbation theory for smoothly deformed surfaces always yields corrections to the interaction of order a^2 . However, for small a/H , the result of Eq. (1.32) has the expansion

$$F_0/A = -\frac{\pi^2}{240} \frac{1}{H^4} \left[1 + 4 \frac{|a|}{H} + \mathcal{O}\left(\left(\frac{a}{H}\right)^2\right) \right] \quad (1.33)$$

which indicates that perturbation theory is not applicable if $\lambda \ll a$. This implies that the apparent divergent behavior for $\lambda \rightarrow 0$ in Eq. (1.28) actually disappears for $\lambda \simeq a$.

1.2.2

Lateral forces

As a natural generalization of the geometry of the previous section, we study the Casimir interaction between two sinusoidally corrugated plates. For direct correspondence to experiments for this type of configuration [22], we consider the specific profiles

$$h_1(y_1) = a \cos(2\pi y_1/\lambda), \quad \text{and} \quad h_2(y_1) = a \cos(2\pi(y_1 + b)/\lambda), \quad (1.34)$$

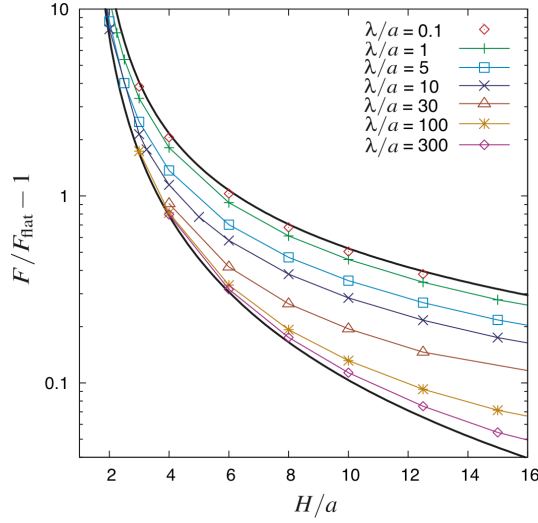


Fig. 1.3 Total Casimir force as function of the mean plate separation H . Shown is the relative change of the force compared to the total Casimir force F_{flat} between two flat plates. The two bold curves enclosing the numerical data are the analytical results F_0 for $\lambda \rightarrow 0$ (upper curve) and F_∞ for $\lambda \rightarrow \infty$ (lower curve), see text.

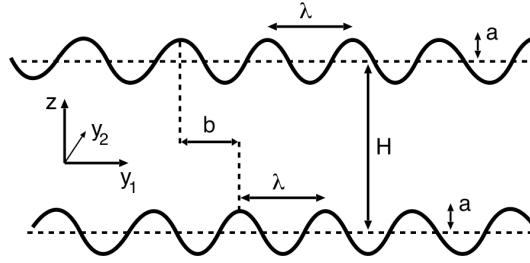


Fig. 1.4 Geometry used for calculating the lateral Casimir force between two corrugated plates with lateral shift b . The equilibrium position is at $b = \lambda/2$.

which are shifted relative to each other by the length b (see Fig. 1.4). When these profiles are substituted into the general expression for the second order term of the partition function of Eq. (1.19) one finds for the Casimir energy

$$\mathcal{E} = \mathcal{E}_0 + 2\mathcal{E}_{\text{cf}} + \mathcal{E}_{\text{cc}}, \quad (1.35)$$

with \mathcal{E}_{cf} given in Eq. (1.24), and where the corrugation-corrugation interaction energy \mathcal{E}_{cc} can be calculated in terms of the kernels $Q_X(\mathbf{y})$ in Eq. (1.19). Besides oscillating contributions to the normal Casimir force from $\mathcal{E}_{\text{cc}}(b)$, a *lateral* force

$$F_{\text{lat}} = -\frac{\partial \mathcal{E}_{\text{cc}}}{\partial b}, \quad (1.36)$$

is induced by the corrugation-corrugation interaction. This lateral force is much better suited for experimental tests of the influence of deformations, since there is no need for subtracting a larger baseline force (the contribution of flat plates) as in the case of the normal force. The lateral force can be also employed as a actuation mechanism in mechanical oscillators as we will see in Section 1.4. In analogy to the previous section, the corrugation-corrugation interaction can be expressed as

$$\mathcal{E}_{cc} = \frac{\hbar c a^2}{H^5} \cos\left(\frac{2\pi b}{\lambda}\right) \left[J_{\text{TM}}\left(\frac{H}{\lambda}\right) + J_{\text{TE}}\left(\frac{H}{\lambda}\right) \right] + \mathcal{O}(a^3) \quad (1.37)$$

with

$$\begin{aligned} J_{\text{TM}}(x) = & \frac{\pi^2}{120} (16x^4 - 1) \operatorname{arctanh}(\sqrt{u}) + \sqrt{u} \left[\frac{\pi}{12} \left(x^3 - \frac{1}{80x} \right) \Phi\left(u, 2, \frac{1}{2}\right) \right. \\ & \left. + \frac{x^2}{12} \Phi\left(u, 3, \frac{1}{2}\right) + \frac{x}{16\pi} \Phi\left(u, 4, \frac{1}{2}\right) + \frac{1}{32\pi^2} \Phi\left(u, 5, \frac{1}{2}\right) + \frac{1}{128\pi^3 x} \Phi\left(u, 6, \frac{1}{2}\right) \right], \end{aligned} \quad (1.38)$$

$$\begin{aligned} J_{\text{TE}}(x) = & \frac{\pi^2}{120} (16x^4 - 1) \operatorname{arctanh}(\sqrt{u}) + \sqrt{u} \left[-\frac{\pi}{12} \left(x^3 + \frac{x}{2} + \frac{1}{80x} \right) \right. \\ & \times \Phi\left(u, 2, \frac{1}{2}\right) + \frac{1}{24} \left(x^2 - \frac{3}{4} \right) \Phi\left(u, 3, \frac{1}{2}\right) + \frac{5}{32\pi} \left(x - \frac{1}{20x} \right) \Phi\left(u, 4, \frac{1}{2}\right) \\ & \left. + \frac{7}{64\pi^2} \Phi\left(u, 5, \frac{1}{2}\right) + \frac{7}{256\pi^3 x} \Phi\left(u, 6, \frac{1}{2}\right) \right], \end{aligned} \quad (1.39)$$

where $u \equiv \exp(-4\pi x)$ and $\Phi(z, s, a) = \sum_{k=0}^{\infty} z^k / (a+k)^s$ is the Lerch transcendent. In the limit of large corrugation length, $H/\lambda \rightarrow 0$, this result agrees to lowest order with a pairwise summation approximation where $J_{\text{TM}}(0) + J_{\text{TE}}(0) = \pi^2/120$.

At the other extreme of $\lambda \ll H$, $J_{\text{TM}}(x) + J_{\text{TE}}(x)$ decays *exponentially* fast. This decay distinguishes the lateral force from the normal force. In particular, for large $x = H/\lambda$, we get to leading order

$$J_{\text{TM}}(x) + J_{\text{TE}}(x) = \frac{4\pi^2}{15} (x^4 + \mathcal{O}(x^2)) e^{-2\pi x}. \quad (1.40)$$

Since $J_{\text{TM}}(x) + J_{\text{TE}}(x)$ is positive for all values of x , the equilibrium position of two modulated surfaces is predicted at $b = \lambda/2$. This corresponds to aligning the maxima and minima of the two corrugations (cf. Fig. 1.4).

The numerical approach for computing the functional determinant in the case of periodic surfaces can be also applied to the lateral force [13]. We consider again a rectangular corrugation but now on both surfaces with a lateral shift of b , cf. Fig. 1.5. The numerical results for the lateral force in this geometry are summarized in Figs. 1.5 and 1.6. Fig. 1.5 shows the numerical result for the lateral force for a shift $b = \lambda/4$ and different values of λ/a over more than 4 orders of magnitude for the gap $\delta = H - 2a$, together with two approximate results (PFA and PWS) and the perturbative result for sinusoidal profiles for $\lambda \ll H$. An exponential decay of the force as predicted by perturbation theory can be clearly observed.

The PFA yields a lateral force per unit area $F_{\text{lat,PFA}} = [2\mathcal{E}_0(H) - \mathcal{E}_0(H - 2a) - \mathcal{E}_0(H + 2a)]/\lambda$ for $0 < b < \lambda/2$ where \mathcal{E}_0 has the same meaning as before. $F_{\text{lat,PFA}}$

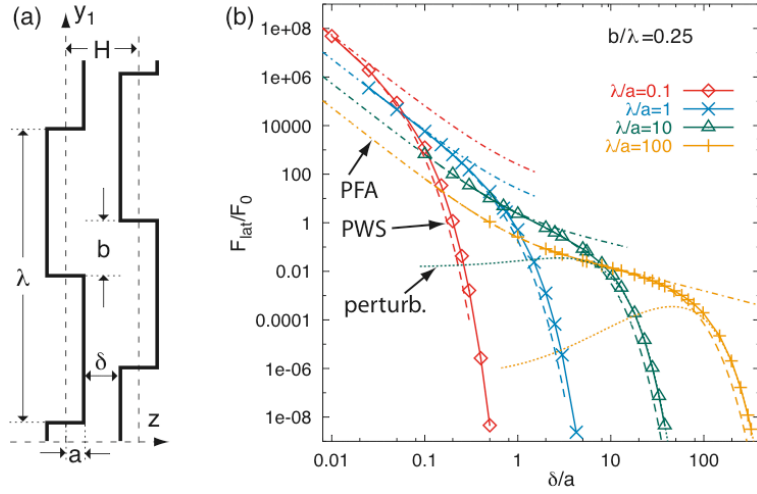


Fig. 1.5 (a) Geometry consisting of two parallel plates with laterally shifted uniaxial rectangular corrugations. (b) Lateral force F_{lat} (in units of normal force F_0 between flat surfaces) at $b = \lambda/4$ for the geometry shown in (a) as function of the gap δ (solid curves). Plotted are also the proximity force (PFA, dash-dotted curves) and pairwise summation (PWS, dashed curves) approximations, and the perturbative result F_{pt} that follows from a calculation for sinusoidal profiles (dotted curves).

changes sign at $b = \lambda/2$ discontinuously which is an artifact of this approximation. The pairwise summation (PWS) of Casimir-Polder potentials is strictly justified for rarefied media only but it is often also applied to metals, using the two-body potential $U(r) = -(\pi/24)\hbar c/r^7$ with the amplitude chosen such as to reproduce the correct result for flat ideal metal plates [7]. It yields a lateral force $F_{\text{lat,PWS}} = -\frac{\partial}{\partial b} \int_{V_l} d^3\mathbf{x} \int_{V_r} d^3\mathbf{x}' U(|\mathbf{x} - \mathbf{x}'|)$ with V_l and V_r denoting the semi-infinite regions to the left and right of the two surfaces in Fig. 1.5(a), respectively. $F_{\text{lat,PWS}}$ can be obtained by numerical integration. For small gaps δ , both approximations agree and match the exact numerical results. Beyond $\delta \gtrsim \lambda/20$ the PFA starts to fail since it does not capture the exponential decay of F_{lat} for increasing δ . The PWS approach has a slightly larger validity range and reproduces the exponential decay. However it deviates by at least *one order of magnitude* from F_{lat} for $\delta \gtrsim 2.5\lambda$.

Although the perturbative result of Eq. (1.37) applies to sinusoidal surfaces, it is instructive to compare it to the numerical results for the rectangular profiles. Since the lateral force decays exponentially, $F_{\text{lat}} \sim e^{-2\pi H/\lambda}$, with the characteristic scale set by the modulation wavelength of the profile, the force at large $H \gg \lambda$ should be determined by the lowest harmonic of the periodic surface profile. This implies a *universal* lateral force for large $H \gg \lambda$ that is independent of the precise form of the surface corrugation. This universal force is the force between two sinusoidal surfaces where the amplitude follows from the projection of an arbitrary periodic profile of wavelength λ onto a sinusoidal profile with the same wavelength. The latter force follows from Eq. (1.37)

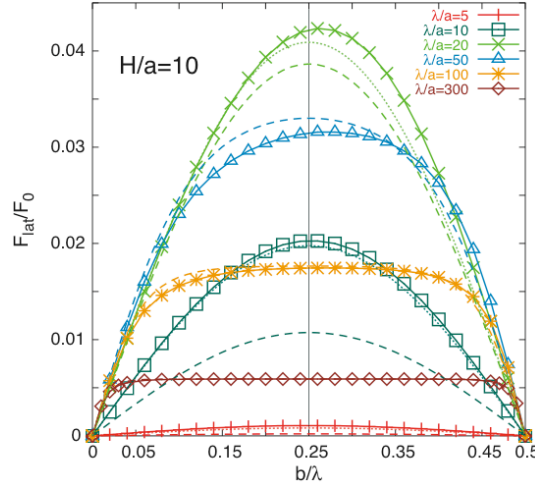


Fig. 1.6 Shape dependence of F_{lat} on the lateral surface shift b at fixed distance $H = 10a$ for different corrugation lengths. The dashed and the dotted curves represent the PWS and the full perturbative result for sinusoidal profiles with arbitrary H/λ , respectively.

and in the limit $\lambda \ll H$ is given by

$$F_{\text{pt}} = \frac{8\pi^3 \hbar c a_0^2 A}{15 \lambda^5 H} \sin\left(\frac{2\pi}{\lambda} b\right) e^{-2\pi H/\lambda}, \quad (1.41)$$

where we assumed an amplitude a_0 for the sinusoidal profiles. For the rectangular corrugation of Fig. 1.5 the lowest harmonic has the amplitude $a_0 = 4a/\pi$. When we compare F_{pt} and the numerical results of Fig. 1.5(b) we find indeed excellent agreement for distances $\delta \gtrsim \lambda$.

The universal behavior of the lateral force is also clearly demonstrated by the dependence of the lateral force on the surface shift b . Corresponding numerical results together with PWS approximations and the force that follows from the *full* perturbative result of Eq. (1.37) for sinusoidal surfaces with arbitrary H/λ are shown in Fig. 1.6 for fixed $H = 10a$ and varying λ/a . With decreasing λ , three regimes can be identified. For $\lambda \gg H$, the force profile resembles almost the rectangular shape of the surfaces, and the PWS approximation yields consistent results. For smaller λ , yet larger than H , the force profile becomes asymmetric with respect to $b = \lambda/4$ and more peaked, signaling the crossover to the universal regime for $\lambda \lesssim H$ where the force profile becomes sinusoidal. In the latter case, for not too small $\lambda/a \approx 10$, the numerical results for F_{lat} indeed agree well with the perturbative result for sinusoidal surfaces with arbitrary H/λ . We note that the PWS approach fails to predict the asymmetry of the force profile, and the PFA even predicts no variation with b for $0 < b < \lambda/2$. To observe this universal behavior of the lateral force experimentally, one should consider surfaces with very small corrugation wavelengths in the range of nanometers so that the exponential decay does not diminish the force for $H \gg \lambda$ too strongly.

1.2.3

Cylinders

In this Section we give examples for two central aspects of fluctuation forces: Effects resulting from the non-additivity and the particular properties of systems with a codimension of two which plays a special role as we will see below. These problems are considered in the context of interactions between cylinders and sidewalls. It has been demonstrated that Casimir forces in these geometries have only a weak logarithmic dependence on the cylinder radius [36] and can be non-monotonic [59, 57, 56] – consequences of codimension and non-additivity. These forces between quasi-one-dimensional structures could be probed in mechanical oscillators that are composed of nano-wires or carbon nanotubes. Exact results for the interaction can be obtained by employing a recently developed scattering approach for Casimir forces [32, 30]. This approach is based on the concept that electromagnetic Casimir interactions result from fluctuating currents inside the bodies. It is possible to formulate an effective action for the multipole moments $\mathbf{Q}_{\alpha,X}$ of the currents inside the bodies where α labels the bodies and X is a multi-index that numbers polarizations (electric and magnetic multipoles) and the elements of the basis for the multipole expansion, e.g., cylindrical waves. The effective action can then be written as the quadratic form

$$S = \sum_{\alpha,\alpha'} \sum_{X,X'} \mathbf{Q}_{\alpha,X}^* \mathbb{M}_{\alpha\alpha',XX'} \mathbf{Q}_{\alpha',X'}, \quad (1.42)$$

with the matrix kernel

$$\mathbb{M}_{\alpha\alpha',XX'} = \kappa \left\{ [(\mathbb{T}_\alpha)^{-1}]_{XX'} \delta_{\alpha\alpha'} - \mathbb{U}_{\alpha\alpha',XX'} (1 - \delta_{\alpha\alpha'}) \right\}, \quad (1.43)$$

where κ is the Wick rotated frequency, $\omega = ic\kappa$, the matrix \mathbb{T}_α is the so-called T-matrix of object α that relates incoming and scattered waves and $\mathbb{U}_{\alpha\alpha'}$ is a “translation” matrix that relates the incoming wave at object α to the outgoing wave at object α' . The T-matrix is related to the scattering matrix of the object, \mathbb{S}_α , by the relation $\mathbb{T}_\alpha = (\mathbb{S}_\alpha - 1)/2$. Analytic results for all elements of the scattering matrix are available for symmetric shapes such as cylinders and spheres. The \mathbb{S}_α matrix contains all information about shape and material composition of the object that is relevant to the Casimir interaction. The translation matrices $\mathbb{U}_{\alpha\alpha'}$ are independent of the properties of the interacting bodies and depend only on the relative position (separation vector) of the objects α and α' and the properties of the fluctuating field. For the electromagnetic field, the translation matrices are known in many bases, e.g., for cylindrical and spherical waves [30]. To obtain the Casimir energy, the multipole fluctuations are integrated out, leading to the determinant of the infinite dimensional matrix \mathbb{M} . Integration over all frequencies κ yields the interaction energy

$$\mathcal{E} = \frac{\hbar c}{2\pi} \int_0^\infty d\kappa \ln \frac{\det \mathbb{M}}{\det \mathbb{M}_\infty}, \quad (1.44)$$

where the division by the determinant of the matrix \mathbb{M}_∞ accounts for the subtraction of the residual energy of the configuration where the separations between all objects tend

to infinity. Since the translation matrices decay to zero with increasing separation, the matrix \mathbb{M}_∞ is given by Eq. (1.43) with the $\mathbb{U}_{\alpha\alpha'}$ set to zero. In the special case of two objects, the energy can be simplified to [32]

$$\mathcal{E}_2 = \frac{\hbar c}{2\pi} \int_0^\infty d\kappa \ln \det(1 - \mathbb{N}), \quad (1.45)$$

where $\mathbb{N} = \mathbb{T}_1 \mathbb{U}_{12} \mathbb{T}_2 \mathbb{U}_{21}$.

First, the scattering approach is applied to two parallel, infinitely long, perfectly conducting cylinders of equal radius R and center-to-center separation d , see Fig. 1.7. For this geometry it is most convenient to use cylindrical vector waves for the multipole expansion. This basis consists of the vector fields $\mathbf{M}_{k_z m}^{i(o)}(\mathbf{x}) = \frac{1}{q} \nabla \times \mathbf{V}^{i(o)}(\mathbf{x})$ for magnetic (M) multipoles and $\mathbf{N}_{k_z m}^{i(o)}(\mathbf{x}) = \frac{c}{q\omega} \nabla \times \nabla \times \mathbf{V}^{i(o)}(\mathbf{x})$ for electric (E) multipoles where $q = \sqrt{(\omega/c)^2 - k_z^2}$ and incoming (i) and outgoing (o) waves differ in the definition of the vector fields $\mathbf{V}^i(\mathbf{x}) = \hat{\mathbf{z}} J_m(qr) e^{im\phi} e^{ik_z z}$, $\mathbf{V}^o(\mathbf{x}) = \hat{\mathbf{z}} H_m^{(1)}(qr) e^{im\phi} e^{ik_z z}$. Here (r, ϕ, z) denote cylindrical coordinates and J_m , $H_m^{(1)}$ are Bessel and Hankel functions of the first kind. In this basis the matrices of Eq. (1.43) assume a simple form where the multi-index X represent now the polarization (M or E), the wave vector k_z along the cylinder axis and the partial wave index m . The T-matrix is diagonal in polarization, k_z and m with diagonal elements

$$T_{Mk_z m} = (-1)^m \frac{\pi}{2i} \frac{I'_m(qR)}{K'_m(qR)} \quad (1.46)$$

$$T_{Ek_z m} = (-1)^m \frac{\pi}{2i} \frac{I_m(qR)}{K_m(qR)}, \quad (1.47)$$

where we have applied a Wick rotation $\omega = ic\kappa$ which leads to modified Bessel functions of the first (I_n) and second (K_n) kind. The translation matrices are diagonal in polarization and k_z , and the elements are identical for both polarizations,

$$U_{12, Mk_z nm} = U_{12, Ek_z nm} = \frac{2}{i\pi} (-i)^{m-n} K_{m-n}(pd) \quad (1.48)$$

$$U_{21, Mk_z nm} = U_{21, Ek_z nm} = \frac{2}{i\pi} i^{m-n} K_{m-n}(pd) \quad (1.49)$$

with $p = \sqrt{\kappa^2 + k_z^2}$. Due to the decoupling of electric and magnetic multipoles, corresponding to transverse magnetic (TM) and transverse electric (TE) field modes, respectively, the Casimir energy of Eq. (1.45) has two independent contributions, $\mathcal{E}_2 = \mathcal{E}_{\text{TM}} + \mathcal{E}_{\text{TE}}$, with

$$\mathcal{E}_{\text{TM(TE)}} = \frac{\hbar c L}{4\pi} \int_0^\infty pdp \ln \det(1 - \mathbb{N}_{\text{TM(TE)}}), \quad (1.50)$$

where L ($\rightarrow \infty$) is the cylinder length and the determinant runs here only over the partial wave indices m, m' of the matrix elements

$$N_{TE, mm'} = i^{m'-m} \sum_n \frac{I'_m(pR)}{K'_m(pR)} K_{n+m}(pd) \frac{I'_n(pR)}{K'_n(pR)} K_{m'+n}(pd) \quad (1.51)$$

$$N_{TM, mm'} = i^{m'-m} \sum_n \frac{I_m(pR)}{K_m(pR)} K_{n+m}(pd) \frac{I_n(pR)}{K_n(pR)} K_{m'+n}(pd). \quad (1.52)$$

This result for the energy can be also obtained from a scalar field theory where TM (TE) modes correspond to Dirichlet (Neumann) boundary conditions [56, 36].

At large separations $d \gg R$, only matrix elements with $m = m' = 0$ for TM modes and $m = m' = 0, \pm 1$ for TE modes contribute to the energy. When the determinant in Eq. (1.50) is restricted to these elements, we find for the interaction of two cylinders for large d/R to leading order

$$\begin{aligned}\mathcal{E}_{\text{TM}} &= -\hbar c L \frac{1}{8\pi} \frac{1}{d^2 \ln^2(d/R)} \left(1 - \frac{2}{\ln(d/R)} + \dots \right), \\ \mathcal{E}_{\text{TE}} &= -\hbar c L \frac{7}{5\pi} \frac{R^4}{d^6}.\end{aligned}\quad (1.53)$$

The asymptotic interaction is dominated by the contribution from TM modes that vanishes for $R \rightarrow 0$ only logarithmically.

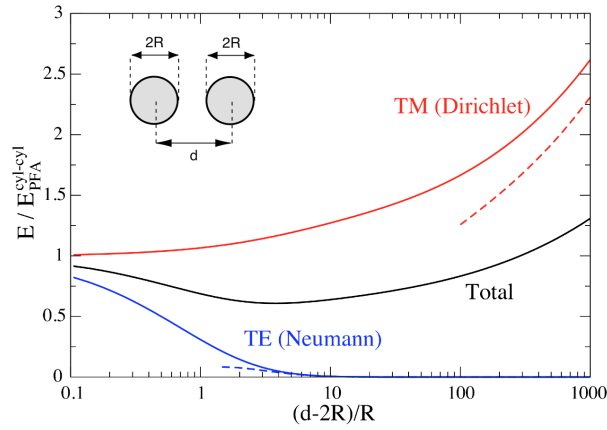


Fig. 1.7 Casimir energy for two cylinders of equal radius R as a function of surface-to-surface distance $d - 2R$ (normalized by the radius). The energy is divided by the PFA estimate

$E_{\text{PFA}}^{\text{cyl-cyl}} = -\frac{\pi^3}{1920} \hbar c L \sqrt{R} / (d - 2R)^{5/2}$ for the energy which is applicable in the limit $d \rightarrow 2R$ only. The solid curves show numerical results; the dashed lines represent the asymptotic results of Eq. (1.53). The inverse logarithmic correction to the leading order result for TM modes cause very slow convergence. For the parameter range shown here it was sufficient to consider $m = 40$ partial waves to obtain convergence.

For arbitrary separations higher order partial waves have to be considered. The number of partial waves has to be increased with decreasing separation. A numerical evaluation of the determinant and integration has revealed an exponentially fast convergence of the energy in the truncation order for the partial waves, leading to the results shown in Fig. 1.7 [56]. It should be noted that the minimum in the curve for the total electromagnetic energy results from the scaling by the PFA estimate of the energy. The total energy is monotonic and the force attractive at all separations.

The interaction between cylinders is very distinct from the Casimir or van der Waals interaction which is reported in literature [55]. Usually, the interaction is proportional to the volumes of the interacting objects, i.e., for two spheres of radius R where the Casimir energy $\sim R^6/d^7$. This scaling with volumes follows also from a pairwise summation of two-body forces. However, from the interaction of two parallel plates one knows that the interaction can scale also with the surface area. This two examples would suggest for two parallel cylinders of length L an interaction energy $\sim LR^4/d^6$ or $\sim LR^2/d^4$. But the actual results of Eq. (1.53) has a much weaker, only logarithmic dependence on the radius. It is interesting to look at the variation of the decay exponent of d for the Casimir energy as a function of the codimension of the object. The exponent is $(-3, -2 + \epsilon, -7)$ for codimensions 1 (plates), 2 (cylinders), 3 (spheres), respectively, and hence *not monotonic*. For a codimension of two, the Casimir interaction is most long ranged. The physical reason for the unexpected scaling of the cylinder interaction is explained by considering spontaneous charge fluctuations. On a sphere, the positive and negative charges can be separated by at most distances of order $R \ll d$. The retarded van der Waals interactions between the dipoles on the spheres lead to the Casimir–Polder interaction [15]. In the cylinder, fluctuations of charge along the axis of the cylinder can create arbitrary large positively (or negatively) charged regions. The retarded interaction of these charges (not dipoles) gives the dominant term of the Casimir force. This interpretation is consistent with the difference between the two types of polarizations, since for TE modes such charge modulations cannot occur due to the absence of an electric field along the cylinder axis, cf. Eq. (1.53) and Fig. 1.7.

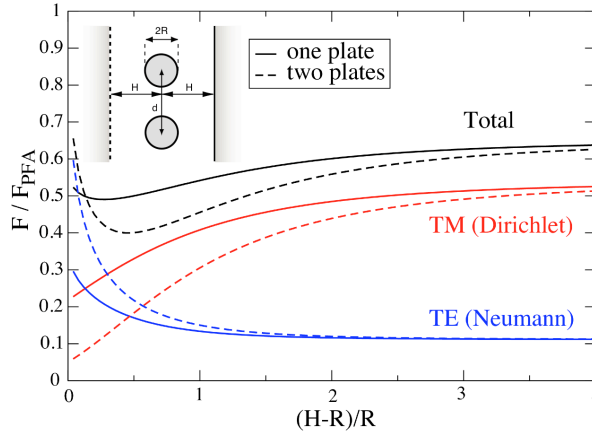


Fig. 1.8 Casimir force between two cylinders parallel to one plate or sandwiched between two plates vs. the ratio of sidewall separation to cylinder radius $(H - R)/R$, at fixed distance $d = 4R$ between the cylinders, normalized by the total PFA force per unit length between two isolated cylinders, $F_{\text{PFA}} = -\frac{5}{2}(\hbar c \pi^3 / 1920) \sqrt{R/(d - 2R)^7}$. The solid lines refer to the case with one plate, while dashed lines depict the results for two plates. Also shown are the individual TE (blue) and TM (red) contributions to the force.

As a second example, the effect of sidewalls on the interaction of two cylinders is considered. The geometry consisting of either one or two plates at a separation H from the two cylinders is shown in Fig. 1.8. For this type of geometry the mean stress tensor has been computed numerically and it has been observed that the force between two one-dimensional structures changes nonmonotonically when H is increased [59, 57]. This many-body effect can be studied by the scattering approach. Instead of studying directly the interaction of the cylinders and plates via their T-matrices, it is more convenient to employ the method of images to describe the effect of the sidewalls [30, 56]. For perfectly conducting sidewalls, their effect on the electromagnetic field can be taken into account by replacing the free space Green's function by a half-space or slab Green's function. This results in an expression for the Casimir energy similar to Eq. (1.44) that depends only on the T-matrices of the two cylinders and translation matrices that connect the original cylinders and their mirror images. The expression of the energy can be computed again numerically by truncating the partial wave expansion at sufficiently high order. The resulting Casimir force between two cylinders with one or two sidewalls as function of the sidewall separation H is shown in Fig. 1.8. Two interesting features can be observed. First, the attractive total force varies non-monotonically with H : Decreasing for small H and then increasing towards the asymptotic limit between two isolated cylinders for large H , cf. Eq. (1.53). The extremum for the one-sidewall case occurs at $H - R \approx 0.27R$, and for the two-sidewall case is at $H - R \approx 0.46R$. Second, the total force between the cylinders for the two-sidewall case in the proximity limit $H \rightarrow R$ is larger than for $H/R \rightarrow \infty$. As might be expected, the H -dependence for one sidewall is weaker than for two sidewalls, and the effects of the two sidewalls are not additive: not only is the difference from the $H \rightarrow \infty$ force not doubled for two sidewalls compared to one, but the two curves actually intersect.

A simple generic argument for the non-monotonic sidewall effect has been given in [57]. It arises from a competition between the force from TE and TM polarizations as demonstrated by the results in Fig. 1.8. An intuitive perspective for the qualitatively different behavior of the TE and TM force as a function of the sidewall distance is obtained from the method of images. For the TM polarization (corresponding to Dirichlet boundary conditions in a scalar field theory) the Green's function is obtained by subtracting the contribution from the image so that the image sources have *opposite* signs. Any configuration of fluctuating TM charges on one cylinder is thus screened by images, more so as H is decreased, *reducing* the force on the fluctuating charges of the second cylinder. This is similar to the effect of a nearby grounded plate on the force between two opposite electrostatic charges. Since the reduction in force is present for every charge configuration, it is there also for the average over all configurations.

By contrast, the TE polarization (corresponding to Neumann boundary conditions in a scalar field theory) requires image sources of the *same* sign. The total force between fluctuating sources on the cylinders is now larger and increases as the plate separation H is reduced. Note, however, that while for each fluctuating source configuration, the effect of images is additive, this is not the case for the average over all configurations. More precisely, the effect of an image source on the Green's function is not additive because of feedback effects: the image currents change the surface current distribution,

which changes the image, and so forth. For example, the net effect of the plate on the Casimir TE force *is not* to double the force as $H \rightarrow R$. The increase is in fact larger than two due to the correlated fluctuations.

A similar but weaker non-monotonic dependence on H of the force between the cylinders is also observed for separations d that are different from the particular choice in Fig. 1.8. Also, the force between the cylinders *and the sidewalls* is not monotonic in d but the non-monotonicity is then smaller since the effect of a cylinder on the force between two bodies is smaller than the effect of an infinite plate.

1.2.4 Spheres

So far geometries with a direction of translational invariance have been considered. In the limit of ideal metal surfaces, this invariance lead to a decoupling of the two polarizations of the electromagnetic field. Any geometry of experimental interest will obviously lack this symmetry beyond some length scale. Hence, it is important to study geometries without this symmetry. *Compact* objects of arbitrary shape obviously do not have an invariant direction. Therefore, the two polarisations are coupled and the matrices in Eq. (1.43) assume a more complicated form. A natural choice for a basis are now vector spherical waves for which the translation matrices $\mathbb{U}_{\alpha\alpha',XX'}$ carry an index $X = (E \text{ or } M, l, m)$ which represents polarisation E or M and the order $l \geq 1, m = -l, \dots, l$ of the spherical waves. In contrast to the cylindrical matrices of Eq. (1.48), the translation matrix couples now E and M polarisation and all matrix elements are known explicitly [30].

Here we focus on the simplest case of two compact objects: two perfect metal spheres of equal radius R and center-to-center separation d , see Fig. 1.9. The T-matrix of a dielectric sphere is known from the Mie theory for scattering of electromagnetic waves from spherical particles. Due to spherical symmetry, the E and M polarisations for all l, m are decoupled so that the T-matrix is diagonal and the coupling of polarisations occurs through the translation matrices only. After a Wick rotation to imaginary frequency $\omega = i\epsilon\kappa$ the matrix elements assume in the perfect metal limit the form

$$T_{MMlm'l'm'} = (-1)^l \frac{\pi}{2} \frac{I_{l+\frac{1}{2}}(\kappa R)}{K_{l+\frac{1}{2}}(\kappa R)} \delta_{ll'} \delta_{mm'} \quad (1.54)$$

$$T_{EElm'l'm'} = (-1)^l \frac{\pi}{2} \frac{I_{l+\frac{1}{2}}(\kappa R) + 2\kappa R I'_{l+\frac{1}{2}}(\kappa R)}{K_{l+\frac{1}{2}}(\kappa R) + 2\kappa R K'_{l+\frac{1}{2}}(\kappa R)} \delta_{ll'} \delta_{mm'}. \quad (1.55)$$

Substitution of these matrix elements together with those of $\mathbb{U}_{\alpha\alpha'}$ from [30] in Eq. (1.45) yields the Casimir energy of two spheres. For asymptotically large d , the energy has only contributions from $l = l' = 1$ (dipoles) and one obtains the Casimir-Polder interaction between two polarizable particles [15] where the electric and magnetic dipole polarizabilities of a perfect metal sphere are given by $\alpha_E = R^3$ and $\alpha_M = -R^3/2$. This result can be extended to smaller separations by including higher order multipoles with $l > 1$ that generate higher powers of R/d . One obtains the asymptotic

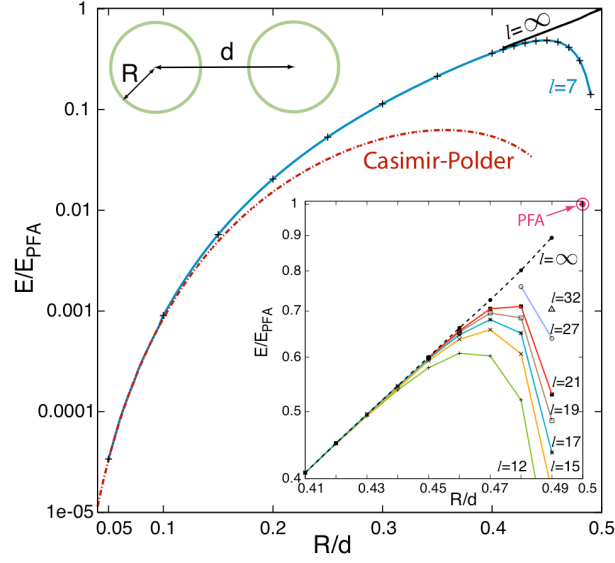


Fig. 1.9 Casimir energy of two metal spheres, divided by the PFA estimate $\mathcal{E}_{\text{PFA}} = -(\pi^3/1440)\hbar c R/(d - 2R)^2$, which holds only in the limit $R/d \rightarrow 1/2$. The label l denotes the multipole order of truncation. The curves $l = \infty$ are obtained by extrapolation. The Casimir-Polder curve is the leading term of Eq. (1.56). Inset: Convergence with the truncation order l for partial waves at short separations.

series [32]

$$\mathcal{E}_2 = -\frac{\hbar c}{\pi} \frac{R^6}{d^7} \sum_{n=0}^{\infty} c_n \left(\frac{R}{d}\right)^n, \quad (1.56)$$

where the first 8 coefficients are $c_0=143/16$, $c_1=0$, $c_2=7947/160$, $c_3=2065/32$, $c_4=27705347/100800$, $c_5 = -55251/64$, $c_6 = 1373212550401/144506880$, $c_7 = -7583389/320$. The energy at all separations can be obtained by truncating the matrix \mathbb{N} defined below Eq. (1.45) at a finite multipole order l , and by computing the determinant and the integral numerically. The result is shown in Fig. 1.9. It provides the force for all separations between the Casimir-Polder limit for $d \gg R$, and the PFA result for $R/d \rightarrow 1/2$. At a surface-to-surface distance $4R/3$ ($R/d = 0.3$), the PFA overestimates the energy by a factor of 10. Including up to $l = 32$ partial wave orders and extrapolating based on an exponential convergence in l , the Casimir energy has been determined down to $R/d = 0.49$ [32]. The interaction between a sphere and a plate has been obtained recently and deviations from the PFA have been quantified [30].

1.3

Dependence on material properties

In the previous Sections we have considered perfectly conducting bodies. For real metals with finite, frequency dependent conductivity, or more general dielectric media, Casimir interactions are modified. This is a natural consequence of the fact that dipole and higher multipole polarizabilities depend on the material properties of a body. Thus, the induced fluctuating currents depend not only on shape but also on material composition. For practical applications and experimental tests it is therefore important to understand the collective effects of shape and material on Casimir interactions. A macroscopic theory that fully accounts for the material dependence of the interaction between two *planar* surfaces has been established by Lifshitz [47] in 1956. Until recently, only approximations, limited to short separations between bodies or sufficiently diluted media, have been available to study the interaction of dielectric media of arbitrary shapes. The scattering approach described in the previous Section has paved the way for studying in detail the material and shape dependence of Casimir forces beyond the case of planar surfaces and without the common approximations. We first provide a simple derivation of the Lifshitz result for two surfaces within the scattering approach. Then we focus on an example that is of particular interest to the behavior of nano-particles as they appear, i.e., in suspensions where correlations between material and shape effects are important.

1.3.1

Lifshitz formula

Consider two material halfspaces that are bounded by planar, parallel surfaces with a vacuum gap of width d between them. The material in the two halfspaces can be different and is characterized by the dielectric functions $\epsilon_\alpha(\omega)$ and magnetic permeabilities $\mu_\alpha(\omega)$ where $\alpha = 1, 2$ numbers the halfspaces. A compact derivation of the Casimir-Lifshitz interaction between the two surfaces follows from the scattering formula of Eq. (1.44). The T-matrix of a planar dielectric surface is given by the Fresnel coefficients which are usually expressed in a planar wave basis. When we define the two polarizations relative to the surface normal vector, the T-matrix is diagonal in polarization and in the wave vector k_\parallel parallel to the surface. The diagonal matrix elements are

$$\begin{aligned} T_{\alpha, M k_\parallel} &= \frac{\mu_\alpha(i\kappa)p - p_\alpha}{\mu_\alpha(i\kappa)p + p_\alpha}, \\ T_{\alpha, E k_\parallel} &= \frac{\epsilon_\alpha(i\kappa)p - p_\alpha}{\epsilon_\alpha(i\kappa)p + p_\alpha} \end{aligned} \quad (1.57)$$

where $p = \sqrt{\kappa^2 + k_\parallel^2}$ and $p_\alpha = \sqrt{\epsilon_\alpha(i\kappa)\mu_\alpha(i\kappa)\kappa^2 + k_\parallel^2}$. The translation matrices for translations perpendicular to the surfaces by a distance d are also diagonal in k_\parallel in the planar wave basis and the diagonal elements have the simple form

$$U_{\alpha\alpha', M k_\parallel} = U_{\alpha\alpha', E k_\parallel} = e^{-pd} \quad (1.58)$$

for $\alpha \neq \alpha' = 1, 2$, i.e., they do not couple E and M polarizations and are identical for the two polarizations. The determinant of Eq. (1.44) leads to a product over all k_{\parallel} which becomes an integral after taking the logarithm. The resulting Casimir-Lifshitz energy has two separate contributions from M and E polarizations (TE and TM modes, respectively),

$$\begin{aligned} \mathcal{E} = & \frac{\hbar c A}{4\pi^2} \int_0^{\infty} d\kappa \int_0^{\infty} k_{\parallel} dk_{\parallel} \ln \left[\left(1 - \frac{\epsilon_1(i\kappa)p - p_1}{\epsilon_1(i\kappa)p + p_1} \frac{\epsilon_2(i\kappa)p - p_2}{\epsilon_2(i\kappa)p + p_2} e^{-2pd} \right) \right. \\ & \left. \times \left(1 - \frac{\mu_1(i\kappa)p - p_1}{\mu_1(i\kappa)p + p_1} \frac{\mu_2(i\kappa)p - p_2}{\mu_2(i\kappa)p + p_2} e^{-2pd} \right) \right], \end{aligned} \quad (1.59)$$

where A is the surface area. This results generalizes the Casimir interaction between two perfect metal plates of Eq. (1.5) to dielectric materials.

1.3.2

Nanoparticles: quantum size effects

The Lifshitz formula of Eq. (1.59), while derived for infinitely extended planar surfaces, is commonly applied within a proximity approximation also to curved surfaces of particles of finite size. This leads to predictions for the interaction that are limited to particles that are very large compared to their separations. To be able to study the interaction of particles of arbitrary sizes and separations, a theory is needed that is a generalization of the Lifshitz formula to bodies of arbitrary shape. Such a general theory provides the scattering formula of Eq. (1.44). The challenges in applying this formula consist in the computation of the T-matrix for bodies with general dielectric functions and in the proper modelling of the dielectric response of the bodies. The latter is especially important for nano-particles for which bulk optical properties are modified by finite-size effects.

Some characteristic effects of the Casimir interaction between nano-particles will be discussed in this Section by studying two spheres with *finite* conductivity in the limit where their radius R is much smaller than their separation d . We assume further that R is large compared to the inverse Fermi wave vector π/k_F of the metal. Since typically π/k_F is of the order of a few Angstrom, this assumption is reasonable even for nano-particles. To employ Eq. (1.44), we need the T-matrix of a sphere with general dielectric function $\epsilon(\omega)$ which generalizes the matrix of Eqs. (1.54), (1.55). All elements of this matrix are known explicitly, see, e.g., [32]. Relevant to the interaction for $d \gg R$ are the dipole matrix elements ($l = l' = 1$) at low frequencies κ . To proceed, we need information about the dielectric function on the imaginary frequency axis $\omega = i\kappa$ for small κ . Theories for the optical properties of small metallic particles [62] suggest a Drude like response

$$\epsilon(i\kappa) = 1 + 4\pi \frac{\sigma(i\kappa)}{c\kappa}, \quad (1.60)$$

where $\sigma(i\kappa)$ is the conductivity which approaches for $\kappa \rightarrow 0$ the dc conductivity σ_{dc} . For bulk metals $\sigma_{dc} = \omega_p^2 \tau / 4\pi$ where $\omega_p = \sqrt{4e^2 k_F^3 / 3\pi m_e}$ is the plasma frequency with electron charge e and electron mass m_e , and τ is the relaxation time. With

decreasing dimension of the particle, $\sigma_{dc}(R)$ is reduced compared to its bulk value due to finite size effects and hence becomes a function of R [62].

In the low frequency limit, with $\epsilon(ic\kappa)$ of Eq. (1.60) the T-matrix elements for magnetic and electric dipole scattering ($l = l' = 1$) are diagonal in m and have the series expansion

$$T_{MM\ 1m\ 1m} = -\frac{4\pi}{45} \frac{R\sigma_{dc}(R)}{c} (\kappa R)^4 + \dots \quad (1.61)$$

$$T_{EE\ 1m\ 1m} = \frac{2}{3} (\kappa R)^3 - \frac{1}{2\pi} \frac{c}{R\sigma_{dc}(R)} (\kappa R)^4 + \dots \quad (1.62)$$

To leading order $\sim \kappa^3$ the electric dipole matrix elements are identical to those of a perfectly conducting sphere and finite conductivity modifies higher orders only. In the magnetic dipole matrix elements, however, the leading term $-(\kappa R)^3/3$ of the perfect conductor result of Eq. (1.54) is absent. This is consistent with the observation that the magnetic dipole polarizability is reduced by a factor $\sim (\kappa R)^2[\epsilon(ic\kappa) - 1]$ and $\epsilon(ic\kappa) - 1 \sim \kappa^{-1}$ due to Eq. (1.60).

When the matrix elements of Eqs. (1.61), (1.62) together with the translation matrices $\mathbb{U}_{\alpha\alpha'}$ in spherical coordinates are substituted into Eq. (1.45) an expansion for large distance d yields the Casimir energy of two spheres

$$\frac{E}{\hbar c} = -\frac{23}{4\pi} \frac{R^6}{d^7} - \left(\frac{R\sigma_{dc}(R)}{c} - \frac{45}{4\pi^2} \frac{c}{R\sigma_{dc}(R)} \right) \frac{R^7}{d^8} + \dots \quad (1.63)$$

The leading term is material independent but different from that of the perfect metal sphere interaction of Eq. (1.56) since only the electric polarization contributes to it. At next order, the first and second terms in the parentheses come from magnetic and electric dipole fluctuations, respectively. Notice that the term $\sim 1/d^8$ is absent in the interaction between perfectly conducting spheres, see Eq. (1.56). The limit of perfect conductivity, $\sigma_{dc} \rightarrow \infty$ cannot be taken in Eq. (1.63) since this limit does not commute with the low κ or large d expansion.

In order to estimate the effect of finite conductivity and its dependence on the size of the nano-particle, we have to employ a theory that can describe the evolution of $\sigma_{dc}(R)$ with the particle size. A theory for the dielectric function of a cubical metallic particle of dimensions $R \gg \pi/k_F$ has been developed within the random phase approximation in the limit of low frequencies $\ll c/R$ [62]. In this theory it is further assumed that the discreteness of the electronic energy levels, and not the inhomogeneity of the charge distribution, is important. This implies that the particle responds only at the wave vector of the incident field which is a rather common approximation for small particles. From an electron number-conserving relaxation time approximation the complex dielectric function is obtained which yields the size-dependent dc conductivity for a cubic particle of volume a^3 [62]. It has been shown that the detailed shape of the particle does not matter much, and we can set $a = (4\pi/3)^{1/3} R$ which defines the volume equivalent

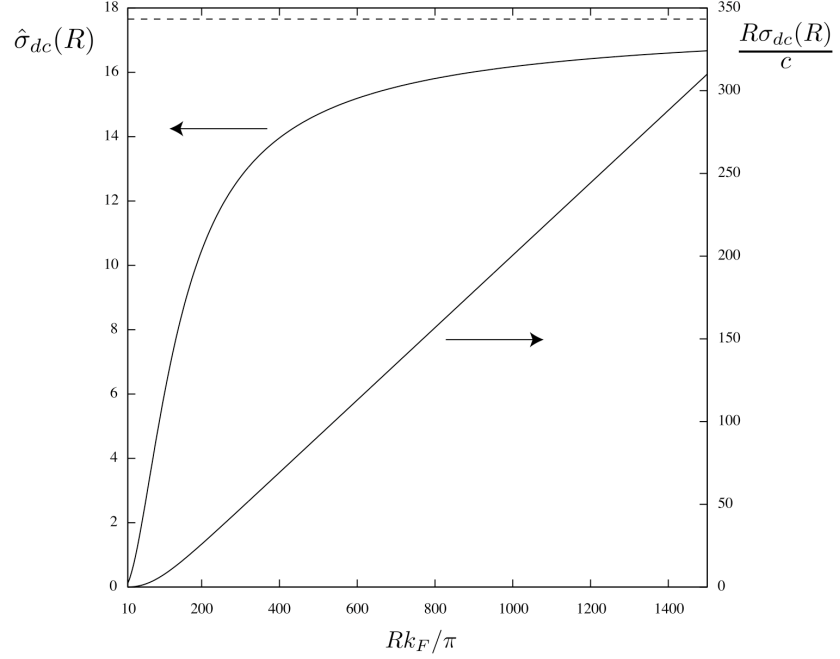


Fig. 1.10 Dimensionless dc conductivity $\hat{\sigma}_{dc}(R)$ in units of $e^2/2\hbar a_0$ (with Bohr radius a_0) for a Aluminum sphere with $\epsilon_F = 11.63\text{eV}$, $\pi/k_F = 1.8\text{\AA}$ and $\tau = 0.8 \cdot 10^{-14}\text{sec}$ as function of the radius R , measured in units of π/k_F , see Eq. (1.64). Also shown is the corresponding ratio $R\sigma_{dc}(R)/c$ that determines the Casimir interaction of Eq. (1.63). The bulk dc conductivity $\hat{\sigma}_{dc}(\infty) = 17.66$ is indicated by the dashed line.

sphere radius R . This yields the estimate

$$\begin{aligned} \sigma_{dc}(R) &= \sigma_{dc}(\infty) \left[1 - \frac{3\pi k_F a + \pi^2}{4(k_F a)^2} - \frac{48\pi}{(k_F a)^3 \Gamma^2} \right. \\ &\quad \left. \times \text{Re} \sum_{m=1}^{k_F a/\pi} m^2 ((k_F a/\pi)^2 - m^2) \times \begin{cases} -z_m \tan z_m & m \text{ even} \\ +z_m \cot z_m & m \text{ odd} \end{cases} \right] \end{aligned} \quad (1.64)$$

with

$$z_m = \frac{\pi m}{2} \sqrt{1 - \frac{i\Gamma}{m^2}} \quad (1.65)$$

and where $\sigma_{dc}(\infty) = \omega_p^2 \tau / 4\pi$ is the bulk Drude dc conductivity and $\Gamma = (\hbar/\tau \epsilon_F)(k_F a/\pi)^2$ is a linewidth with Fermi energy ϵ_F . The factor in square parentheses multiplying $\sigma_{dc}(\infty)$ describes quantum size effects and leads to a substantial *reduction* of the dc conductivity for nano-scale particles. While the above expression is applicable for

$\pi/k_F \ll a$, it suggest that for $\pi/k_F \simeq a$ the particle ceases to be conducting which is consistent with a metal-insulator transition due to the localisation of electrons for particles with a size of the order of the mean free path. It is instructive to consider the size dependence of $\sigma_{dc}(R)$ and of the Casimir interaction for a particular choice of material. Following [62], we focus on small Aluminum spheres with $\epsilon_F = 11.63\text{eV}$ and $\tau = 0.8 \cdot 10^{-14}\text{sec}$. These parameters correspond to $\pi/k_F = 1.8\text{\AA}$ and a plasma wavelength $\lambda_p = 79\text{nm}$. It is useful to introduce the dimensionless conductivity $\hat{\sigma}_{dc}(R)$, which is measured in units of $e^2/2\hbar a_0$ with Bohr radius a_0 , so that the important quantity of Eq. (1.63) can be written as $R\sigma_{dc}(R)/c = (\alpha/2)(R/a_0)\hat{\sigma}_{dc}(R)$ where α is the fine-structure constant. The results following from Eq. (1.64) are shown in Fig. 1.10. For example, for a sphere of radius $R = 10\text{nm}$, the dc conductivity is reduced by a factor ≈ 0.15 compared to the bulk Drude value. If the radius of the sphere is equal to the plasma wavelength λ_p , the reduction factor ≈ 0.8 . These results show that shape and material properties are important for the Casimir interaction between nano-particles. Potential applications include the interaction between dilute suspensions of metallic nano-particles.

1.4

Casimir force driven nanosystems

We have seen that Casimir forces increase strongly with decreasing distance and hence it can be expected that they are important in devices that are composed of moving elements at short separations. Indeed, a common phenomena seen in nano-mechanical devices is stiction due to attractive van der Waals and Casimir forces. This effect imposes a minimum separation between objects in order to prevent that they stick together. However, one can make also good use of Casimir interactions in nano-devices by employing them to actuate components of small devices without contact [1, 29, 2]. In [29] it has been demonstrated that this can be achieved by coupling two periodically structured parallel surfaces by the zero-point fluctuations of the electromagnetic field between them. We will consider this effect here as an example for Casimir force induced non-linear dynamics, providing a direct application of the results obtained in Section 1.2.2. We have seen that the broken translation symmetry parallel to the surfaces results in a sideways force which has been predicted theoretically [34, 35] and observed experimentally between static surfaces [21]. If at least one of the surfaces is structured *asymmetrically* there is an additional breaking of reflection symmetry and the surfaces can in principle be set into relative lateral motion in the direction of broken symmetry. The energy for this transport has to be pumped into the system by external driving. This can be realized by setting the surfaces into relative oscillatory motion so that their normal distance is an unbiased periodic function of time. Since the sideways Casimir force decays exponentially with the normal distance [see Eq. (1.41)], the surfaces experience an asymmetric periodic potential that varies strongly in time.

This scenario resembles so-called ratchet systems [58] that have been studied extensively during the last decade in the context of Brownian particles [41], molecular motors

[3] and vortex physics in superconductors [24], to name a few recent examples. Most of the works on ratchets consider an external time-dependent driving force acting on overdamped degrees of freedom to rectify thermal noise. For nano-systems, however, it has been pointed out that inertia terms due to finite mass should not be neglected and, actually, can help the ratchets to perform more efficiently than their overdamped companions [48]. Finite inertia typically induce in Langevin dynamics deterministic chaos that has been shown to be able to mimic the role of noise and hence to generate directed transport in the absence of external noise [49]. Here we use this effect in the different context of so-called pulsating (or effectively on-off) ratchets where the strengths of the periodic potential varies in time [58]. We consider weak thermal noise only to test for stability of the inertia induced transport — not as the source of driving²⁾.

It has been demonstrated that the system described above indeed allows for directed relative motion of the surfaces due to chaotic dynamics caused by the lateral Casimir force [29]. The transport velocity is stable across sizeable intervals of the amplitude and frequency of surface distance oscillations and damping. The velocity scales linear with frequency across these intervals and is almost constant below a critical mean distance beyond which it drops sharply. The system exhibits multiple current reversals as function of the oscillation amplitude, mean distance and damping. This “Casimir ratchet” allows contact-less transmission of motion which is important since traditional lubrication is not applicable in nano-devices. This actuation mechanism should be compared to other actuation schemes as magnetomotive or capacitive (electrostatic) force transmission. The Casimir effect induced actuation has the advantage of working also for insulators and does not require any electrical contacts and/or external fields. Other applications of zero-point fluctuation induced (van der Waals) interactions to nano-devices have been experimentally realized already to construct ultra-low friction bearings from multiwall carbon nanotubes [23].

In the following, we consider two (on average) parallel metallic surfaces with periodic, uni-axial corrugations (along the y_1 -axis) that have distance H , see inset (a) of Fig. 1.11. To begin with, we assume that both surfaces are at rest with a relative lateral displacement b . Then the surface profiles can be parametrized as

$$h_1(y_1) = a \sum_{n=1}^{\infty} c_n e^{2\pi i n y_1 / \lambda_1} + \text{c.c.}, \quad (1.66)$$

$$h_2(y_1) = a \sum_{n=1}^{\infty} d_n e^{2\pi i n (y_1 - b) / \lambda_2} + \text{c.c.}, \quad (1.67)$$

where a is the corrugation amplitude, λ_1, λ_2 are the corrugation wave lengths, c_n, d_n are Fourier coefficients.

The dependence of the Casimir energy \mathcal{E} on H and b causes macroscopic forces on the surfaces. For a varying separation H this is the normal Casimir attraction between metallic surfaces, modified by the corrugations. Below we will assume $H = H(t)$ to be a time-dependent distance that is kept at a fixed oscillation by an additional external

²⁾In the absence of inertia, finite thermal noise is necessary for on-off ratchets to generate directed motion.

force from clamping to an oscillator. In such setup, the surfaces can react freely only to the lateral force component $\mathcal{F}_{\text{lat}}(b, H) = -\partial\mathcal{E}/\partial b$. The results of Section 1.2.2 are readily extended to periodic profiles of arbitrary shapes as described by Eq. (1.66). The corrugation lengths have to be commensurate, $\lambda_1/\lambda_2 = p/q$ with integers p, q in order to produce a finite lateral force per surface area. For the purpose of this example, it is sufficient to consider the case $p = 1$. Generalizing the result of Eq. (1.37), the lateral (b -dependent) part of the Casimir energy per surface area can then be written as

$$\mathcal{E}(b) = \frac{2\hbar c a^2}{H^5} \sum_{n=1}^{\infty} \left(c_n d_{-nq} e^{-2\pi i n b / \lambda_1} + \text{c.c.} \right) J\left(n \frac{H}{\lambda_1}\right) \quad (1.68)$$

to order a^2 . The exact form of the function $J(x) = J_{\text{TM}}(x) + J_{\text{TE}}(x)$ is given by Eqs. (1.38), (1.39). For the present purpose it is sufficient to use the simplified expression

$$J(x) \simeq \frac{\pi^2}{120} (1 + 2\pi x + \gamma x^2 + 32x^4) e^{-2\pi x} \quad (1.69)$$

with $\gamma = 12.4133$, which is exact for both asymptotically large and small x and approximates the exact results with sufficient accuracy for all x . (The maximal deviation from the exact result is $\approx \pm 0.5\%$ around $x = 0.5$.) The Casimir potential of Eq. (1.68) has two interesting properties which are useful to the construction of a ratchet. First, it decays exponentially with H , and thus can be essentially switched on and off periodically in time by oscillating H . Second, the potential is not only periodic in b but acquires asymmetry from the surface profiles at small $H \ll \lambda$ and an universal symmetric shape for $H \gg \lambda$ since the effect of higher harmonics of the surface profile is exponentially diminished as discussed in Section 1.2.2.

The relative surface displacement $b(t)$ can be considered as a classical degree of freedom with inertia. Its equation of motion is described by Langevin dynamics of the form

$$\rho \ddot{b} + \gamma \rho \dot{b} = \mathcal{F}_{\text{lat}}[b, H(t)] + \sqrt{2\gamma\rho T} \xi(t), \quad (1.70)$$

where ρ is the mass per surface area, γ the friction coefficient, T the intensity (divided by surface area) of the Gaussian noise $\xi(t)$ with zero mean and correlations $\langle \xi(t)\xi(t') \rangle = \delta(t - t')$ so that the Einstein relation is obeyed. This stochastic term describes ambient noise due to effects of temperature and pressure. (Additional contributions from thermally excited photons to the Casimir force can be neglected at surface distances well below the thermal wavelength $\hbar c/(2T)$.) The system is driven by rigid oscillations of one surface so that the distance $H(t) = H_0 g(t)$ oscillates about the mean distance H_0 with $g(t) = 1 - \eta \cos(\Omega t)$. For simplicity, we consider now equal corrugation lengths $\lambda_1 = \lambda_2 \equiv \lambda$. We define the following dimensionless variables: $\hat{b} = b/\lambda$, $s = t/\tau$ for lateral lengths and time with the typical time scale $\tau = (\lambda/a)\sqrt{\rho H_0^5/\hbar c}$ resulting from a balance between inertia and Casimir force. Hence velocities will be measured in units of $v_0 = \lambda/\tau$. There are five dimensionless parameters which can be varied independently for fixed surface profiles: the damping $\hat{\gamma} = \tau\gamma$, the angular frequency $\omega = \tau\Omega$, the driving amplitude η , the scaled mean distance H_0/λ and the noise intensity $\hat{T} = (T/\hbar c)(H_0^5/a^2)$. The dimensionless equation of motion for $\hat{b}(s)$ reads

$$\ddot{\hat{b}} + \hat{\gamma} \dot{\hat{b}} = \hat{\mathcal{F}}_{\text{lat}}[\hat{b}, \hat{g}(s)] + \sqrt{2\hat{\gamma}\hat{T}} \hat{\xi}(s) \quad (1.71)$$

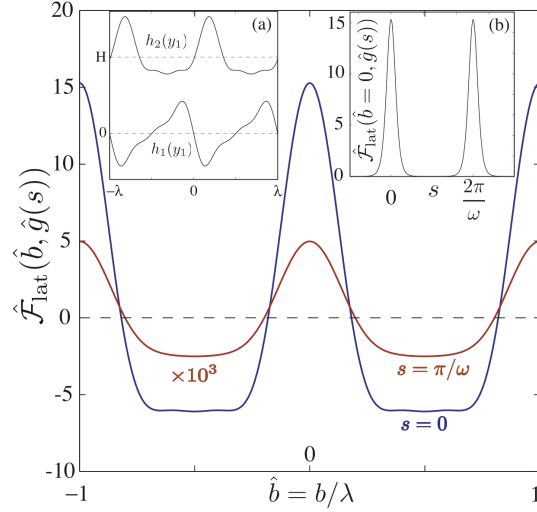


Fig. 1.11 The lateral Casimir force acting between the two surfaces as function of the shift \hat{b} at time $s = 0$ and half period $s = \pi/\omega$ (drawn to a larger scale by a factor 10^3) for parameters $\eta = 0.65$, $H_0 = 0.1\lambda$. Insets: (a) Surface profiles at their equilibrium position at $\hat{b} = 0.182$ (b) Periodic variation of the maximum force at $\hat{b} = 0$ with time.

with the Casimir force

$$\hat{\mathcal{F}}_{\text{lat}}(\hat{b}, \hat{g}) = \frac{4\pi}{\hat{g}^5} \sum_{n=1}^{\infty} f_n \cos(2\pi n \hat{b}) J\left(n \hat{g} \frac{H_0}{\lambda}\right), \quad (1.72)$$

where we have chosen surface profiles with $c_n = i\sqrt{f_n/(2n)}$, $d_n = \sqrt{f_n/(2n)}$ with real coefficients f_n in Eq. (1.66), and $\hat{g}(s) = 1 - \eta \cos(\omega s)$.

Directed transport is possible in certain parameter ranges even in the deterministic case where noise is absent. However, to probe the robustness of transport, we consider in the following primarily the limit of weak noise by choosing $\hat{T} = 10^{-3}$. In fact, it has been shown for underdamped ratchets with time-independent potentials and periodic driving that even an infinitesimal amount of noise can change the rectification from chaotic to stable [48]. To look for similar generic behavior of the pulsating ratchet, we consider a specific geometry consisting of a symmetric and a sawtooth-like surface profile corresponding to three harmonics with $f_1 = 0.0492$, $f_2 = 0.0241$, $f_3 = 0.0059$ and $f_n = 0$ for $n > 3$. Inset (a) of Fig. 1.11 shows these profiles in their stable position with $\hat{b} = 0.182$ that minimizes the Casimir energy. The resulting spatial variation of the Casimir force with \hat{b} is plotted in Fig. 1.11 for minimal ($s = 0$) and maximal ($s = \pi/\omega$) surface distance with parameters $H_0/\lambda = 0.1$, $\eta = 0.65$. It can be clearly seen that the asymmetry is reduced at larger distance where the variation of the force becomes more sinusoidal. Inset (b) shows the on-off-like time-dependence of the force amplitude at $\hat{b} = 0$ due to the oscillating surface distance.

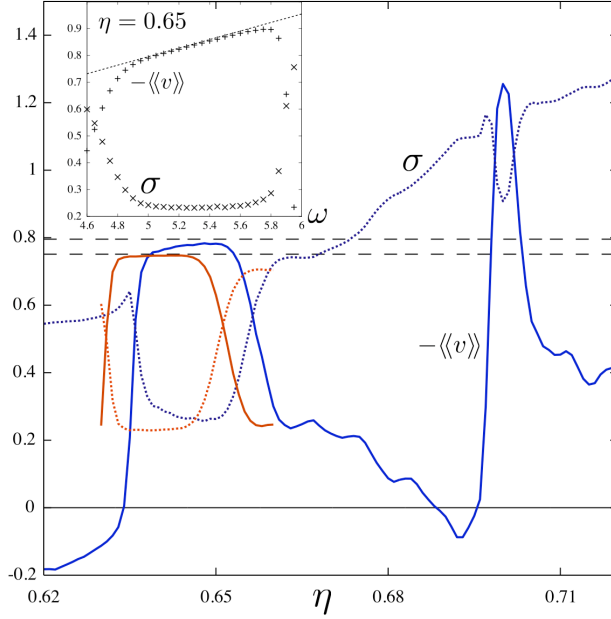


Fig. 1.12 Mean $\langle\langle v \rangle\rangle$ and standard deviation σ of the (negative) velocity as function of the driving amplitude η for the frequencies $\omega = 5.0$ and $\omega = 4.72$ (for the latter only the stable plateau is shown). The parameters are $H_0 = 0.1\lambda$, $\hat{\gamma} = 0.9$, $T = 10^{-3}$. Inset: Dependence of the same quantities on frequency for fixed $\eta = 0.65$. Straight dashed lines correspond in both graphs to the velocity $\omega/(2\pi)$.

The non-linear equation of motion of Eq. (1.71) has to be solved numerically. The trajectory $\hat{b}(s)$ was obtained from a second order Runge-Kutta algorithm. As initial conditions an equidistant distribution over the interval $[-1, 1]$ for $\hat{b}(0)$ and $\dot{\hat{b}}(0) = 0$ is used. For each set of parameters 200 different trajectories are calculated from varying initial conditions and noise, each evolving over 4×10^3 periods $2\pi/\omega$ so that transients have decayed. The average velocity $\langle\langle v \rangle\rangle$ involves two different averages of $\dot{\hat{b}}(s)$: The first average is over initial conditions and noise for every time step, then the averaged trajectory is averaged over all discrete times of the numerical solution. For an efficient directed transport it is not sufficient to have only a finite average $\langle\langle v \rangle\rangle$. To exclude trajectories with a high number of velocity reversals, the fluctuations about the average velocity must be small, i.e., the variance $\sigma^2 = \langle\langle v^2 \rangle\rangle - \langle\langle v \rangle\rangle^2$ must be smaller than $\langle\langle v \rangle\rangle^2$.

Naively, one can expect directed motion of the surface profile $h_2(y_1)$ into the positive y_1 -direction ($\dot{\hat{b}} < 0$) since the Casimir force in Fig. 1.11 is asymmetric with negative values lasting for longer time than positive ones. However, the actual behavior is more complicated due to chaotic dynamics. Fig. 1.12 shows the dependence of the average

velocity and its standard deviation σ on the driving amplitude η and frequency ω for $H_0 = 0.1\lambda$, $\hat{\gamma} = 0.9$. For a fixed frequency there is an optimal interval of driving amplitudes across which the average velocity is almost constant with $\langle\langle v \rangle\rangle \simeq -\omega/(2\pi)$. Small deviations from the latter value result from noise as has been checked by studying the dynamics at $\hat{T} = 0$. At higher driving amplitudes a second narrower interval with maximal $\langle\langle v \rangle\rangle$ is observed which is more strongly reduced and smeared out from its deterministic value $-2 \times \omega/(2\pi)$ by noise. At the plateaus of constant velocity the standard deviation σ is substantially reduced, rendering transport efficient. Outside the plateaus velocity reversals occur and σ increases linearly with η . For fixed amplitude η , the average velocity is stable at the value $-\omega/(2\pi)$ over a sizeable frequency range (see inset of Fig. 1.12).

In order to understand the observed behavior it is instructive to analyze the dynamics in the three dimensional extended phase space. Attractors of the long-time dynamics can be identified from Poincaré sections using the period $2\pi/\omega$ of the surface oscillation as stroboscopic time. To obtain a compact section, the trajectory is folded periodically in y_1 on one period of the Casimir potential. From these sections we can distinguish between periodic and chaotic orbits. As a start, we consider the deterministic limit with $\hat{T} = 0$. The plateaus around $\eta = 0.65$ and $\eta = 0.7$ result both from periodic orbits of period one, corresponding to a single point in the Poincaré section. On the right (downward) edges of the first plateaus we observe period doubling, i.e., a periodic attractor with period two. Upon a further increase of η , chaotic orbits dominate the motion. Hence the system exhibits a period-doubling route to chaos with enhanced velocity fluctuations. The findings apply basically also to weak noise ($\hat{T} = 10^{-3}$) but the sharp points of the periodic attractors in the Poincaré sections are smeared out leading to a decreased $\langle\langle v \rangle\rangle$. The transition from chaotic to periodic dynamics at the beginning of the rising edge of the plateaus is accompanied by a velocity reversal. This is consistent with the observation for non-pulsating potentials that velocity reversals are due to a bifurcation from chaotic to periodic dynamics [49].

The amplitude of the Casimir potential can be tuned by varying the mean distance H_0 . From Fig. 1.13(a) we see that the dynamics show a sharp transition at a critical H_0/λ from efficient transport with large $\langle\langle v \rangle\rangle$ and small σ to chaotic dynamics with vanishing velocity. The transition is accompanied by a velocity reversal and peaked velocity fluctuations. Interestingly, below the transition $\langle\langle v \rangle\rangle$ is almost constant independently of H_0/λ . The observed transport behavior is also stable against a change of effective damping $\hat{\gamma}$ as shown in Fig. 1.13(b). Whereas fluctuations increase with decreasing $\hat{\gamma}$, there is a stable plateau of constant average velocity across which fluctuations are diminished. In the deterministic limit, additional plateaus with inverted and doubled average velocity are observed by varying $\hat{\gamma}$ and η . Remnants of a second plateau around $\hat{\gamma} = 1.9$, washed out by noise, can be seen in Fig. 1.13(b).

It is interesting to estimate typical velocities $v_0 = \lambda/\tau$. With the typical lengths $H_0 = 0.1\mu\text{m}$, $a = 10\text{nm}$ realized in recent Casimir force measurements [21] and an area mass density of $\rho = 10\text{g/m}^2$ for silicon plates with a thickness of a few microns, one obtains $v_0 = \sqrt{\hbar c a^2 / \rho H_0^5} \approx 5.5\text{mm/s}$. The actual average velocity $v_0\omega/2\pi$ is of the same order for the frequencies studied above. For $\lambda = 1\mu\text{m}$, the time scale is

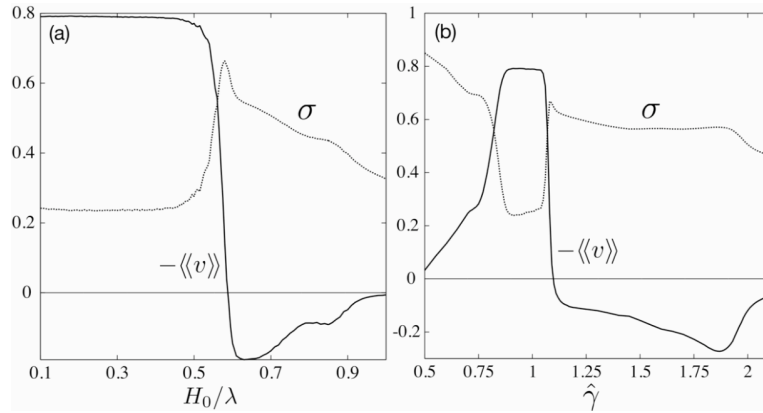


Fig. 1.13 Mean $\langle\langle v \rangle\rangle$ and standard deviation σ of the (negative) velocity as function of (a) the mean plate distance H_0 for $\hat{\gamma} = 0.9$ and (b) damping $\hat{\gamma}$ for $H_0 = 0.1\lambda$. The other parameters are $\eta = 0.65$, $\omega = 5.0$, $\hat{T} = 10^{-3}$.

$\tau = \lambda/v_0 \approx 10^{-4}$ s leading to driving frequencies and damping rates in the kHz range for the parameters considered here.

The results show that Casimir interactions can offer novel contact-less translational actuation schemes for nanomechanical systems. Similar ratchet-like effects are expected between objects of different shapes as, e.g., periodically structured cylinders, inducing rotational motion. The use of fluctuation forces appear also promising to move nano-sized objects immersed in a liquid where electrostatic actuation is not possible. Another application is the separation and detection of particles of differing mass adsorbed to the surfaces. For surfaces oscillating at very high frequencies additional interesting phenomena related to the dynamical Casimir effect occur [37], leading to the emission of photons that could contribute to ratchet-like effects as well.

1.5 Conclusion

There has been recent interest in applying Casimir interactions to the design of nanomechanical devices [17, 16, 10, 9, 11]. In such devices as sensors and actuators, attractive Casimir forces can strongly influence their function due to unwanted stiction between small elements at nano-scale separations. But one can make also good use of Casimir interactions in actuators where they can lead to interesting non-linear dynamics. Recently also repulsive Casimir forces between bodies in a liquid, predicted some decades ago by Lifshitz, Dzyaloshinskii and Pitaevskii for planar surfaces [26], have been measured between a sphere and a plane [52], suggesting a way to suppress stiction. Hence it is important to understand the dependence of Casimir forces on shape and material properties beyond common approximations that apply only to weakly curved surfaces.

This conclusion is corroborated by the relevance of Casimir interactions to a plethora of phenomena such as wetting, adhesion, friction, and quantum scattering of atoms from surfaces. In this Chapter, some characteristic effects of shape and material on Casimir interactions have been presented using the examples of geometries that are typical to nanosystems. Most of the presented results could be obtained only recently by newly developed theoretical tools that have been described here. The important study of correlations between shape and material effects and the additional implications of interacting fields in Casimir effects due to critical fluctuations [39] are largely unexplored. It is expected that the recent progress on the experimental and theoretical side will unveil novel phenomena and provide a better understanding of fluctuation induced interactions with interesting implications for nanosystems.

Acknowledgements

Most of the results presented in this chapter have been obtained in collaboration with Noah Graham, Andreas Hanke, Robert L. Jaffe, Mehran Kardar, Sahand Jamal Rahi, and Antonello Scardicchio. Support from the DFG grant No. EM70/3, the Center for Theoretical Physics at MIT, and the MIT-France Seed Fund is gratefully acknowledged.

References

- 1 A. Ashourvan, M. Miri, and R. Golestanian. Noncontact rack and pinion powered by the lateral casimir force. *Phys. Rev. Lett.*, 98:140801, 2007.
- 2 A. Ashourvan, M. Miri, and R. Golestanian. Rectification of the lateral casimir force in a vibrating noncontact rack and pinion. *Phys. Rev. E*, 75:040103, 2007.
- 3 R. D. Astumian and I. Derenyi. Fluctuation driven transport and models of molecular motors and pumps. *Eur. Biophys. J.*, 27:474, 1998.
- 4 R. Balian and B. Duplantier. Electromagnetic waves near perfect conductors. i. multiple scattering expansions. distribution of modes. *Ann. Phys.*, 104:300, 1977.
- 5 R. Balian and B. Duplantier. Electromagnetic-waves near perfect conductors. 2. casimir effect. *Ann. Phys.*, 112:165, 1978.
- 6 M. Bordag. Casimir effect for a sphere and a cylinder in front of a plane and corrections to the proximity force theorem. *Phys. Rev. D*, 73:125018, 2006.
- 7 M. Bordag, U. Mohideen, and V. M. Mostepanenko. New developments in the casimir effect. *Phys. Rep.*, 353:1, 2001.
- 8 G. Bressi, G. Carugno, R. Onofrio, and G. Ruoso. Measurement of the casimir force between parallel metallic surfaces. *Phys. Rev. Lett.*, 88, 2002.
- 9 E. Buks and M. L. Roukes. Metastability and the casimir effect in micromechanical systems. *Europhys. Lett.*, 54:220, 2001.
- 10 E. Buks and M. L. Roukes. Stiction, adhesion energy, and the casimir effect in micromechanical systems. *Phys. Rev. B*, 63:033402, 2001.
- 11 E. Buks and M. L. Roukes. Quantum physics: Casimir force changes sign. *Nature*, 419:119, 2002.
- 12 R. Buscher and T. Emig. Nonperturbative approach to casimir interactions in periodic geometries. *Phys. Rev. A*, 69:062101, 2004.
- 13 R. Buscher and T. Emig. Geometry and spectrum of casimir forces. *Phys. Rev. Lett.*, 94:133901, 2005.
- 14 H. B. G. Casimir. On the attraction between two perfectly conducting plates. *Kon. Ned. Akad. Wetensch. Proc.*, 51:793, 1948.
- 15 H. B. G. Casimir and D. Polder. The influence of retardation on the london-van der waals forces. *Phys. Rev.*, 73:360, 1948.
- 16 H. B. Chan, V. A. Aksyuk, R. N. Kleiman, D. J. Bishop, and F. Capasso. Nonlinear micromechanical casimir oscillator. *Phys. Rev. Lett.*, 87:211801, 2001.
- 17 H. B. Chan, V. A. Aksyuk, R. N. Kleiman, D. J. Bishop, and F. Capasso. Quantum mechanical actuation of microelectromechanical systems by the casimir force. *Science*, 291:1941, 2001.
- 18 H. B. Chan, Y. Bao, J. Zou, R. A. Cirelli, F. Klemens, W. M. Mansfield, and C. S. Pai. Measurement of the casimir force between a gold sphere and a silicon surface

- with nanoscale trench arrays. *Phys. Rev. Lett.*, 101:030401, 2008.
- 19 F. Chen, G. L. Klimchitskaya, V. M. Mostepanenko, and U. Mohideen. Demonstration of the difference in the casimir force for samples with different charge-carrier densities. *Phys. Rev. Lett.*, 97:170402, 2006.
- 20 F. Chen, G. L. Klimchitskaya, V. M. Mostepanenko, and U. Mohideen. Control of the casimir force by the modification of dielectric properties with light. *Phys. Rev. B*, 76:035338, 2007.
- 21 F. Chen, U. Mohideen, G. L. Klimchitskaya, and V. M. Mostepanenko. Demonstration of the lateral casimir force. *Phys. Rev. Lett.*, 88:101801, 2002.
- 22 F. Chen, U. Mohideen, G. L. Klimchitskaya, and V. M. Mostepanenko. Experimental and theoretical investigation of the lateral casimir force between corrugated surfaces. *Phys. Rev. A*, 66:032113, 2002.
- 23 J. Cumings and A. Zettl. Low-friction nanoscale linear bearing realized from multiwall carbon nanotubes. *Science*, 289:602, 2000.
- 24 C. C. de Souza Silva, J. Van de Vondel, M. Morelle, and V. V. Moshchalkov. Controlled multiple reversals of a ratchet effect. *Nature*, 440:651, 2006. 10.1038/nature04595.
- 25 R. S. Decca, D. López, E. Fischbach, G. L. Klimchitskaya, D. E. Krause, and V. M. Mostepanenko. Tests of new physics from precise measurements of the casimir pressure between two gold-coated plates. *Phys. Rev. D*, 75:077101, 2007.
- 26 I. E. Dzyaloshinskii, E. M. Lifshitz, and L. P. Pitaevskii. The general theory of van der waals forces. *Adv. Phys.*, 10:165, 1961.
- 27 T. Ederth. Template-stripped gold surfaces with 0.4-nm rms roughness suitable for force measurements: Application to the casimir force in the 20-100-nm range. *Phys. Rev. A*, 62:062104, 2000.
- 28 T. Emig. Casimir forces: An exact approach for periodically deformed objects. *Europhys. Lett.*, 62:466, 2003.
- 29 T. Emig. Casimir-force-driven ratchets. *Phys. Rev. Lett.*, 98:160801, 2007.
- 30 T. Emig. Fluctuation-induced quantum interactions between compact objects and a plane mirror. *Journal of Statistical Mechanics: Theory and Experiment*, 4:P04007, 2008.
- 31 T. Emig and R. Buscher. Towards a theory of molecular forces between deformed media. *Nucl. Phys. B*, 696:468, 2004.
- 32 T. Emig, N. Graham, R. L. Jaffe, and M. Kardar. Casimir forces between arbitrary compact objects. *Phys. Rev. Lett.*, 99:170403, 2007.
- 33 T. Emig, N. Graham, R. L. Jaffe, and M. Kardar. Casimir forces between compact objects: The scalar case. *Phys. Rev. D*, 77:025005, 2008.
- 34 T. Emig, A. Hanke, R. Golestanian, and M. Kardar. Probing the strong boundary shape dependence of the casimir force. *Phys. Rev. Lett.*, 87:260402, 2001.
- 35 T. Emig, A. Hanke, R. Golestanian, and M. Kardar. Normal and lateral casimir forces between deformed plates. *Phys. Rev. A*, 67(022114), 2003.
- 36 T. Emig, R. L. Jaffe, M. Kardar, and A. Scardicchio. Casimir interaction between a plate and a cylinder. *Phys. Rev. Lett.*, 96:080403, 2006.
- 37 R. Golestanian and M. Kardar. Mechanical response of vacuum. *Phys. Rev. Lett.*, 78:3421, 1997.
- 38 R. Golestanian and M. Kardar. Path-integral approach to the dynamic casimir effect with fluctuating boundaries. *Phys. Rev. A*, 58:1713, 1998.
- 39 C. Hertlein, L. Helden, A. Gambassi, S. Dietrich, and C. Bechinger. Direct measurement of critical casimir forces. *Nature*, 451:172, 2008.
- 40 M. T. Jaekel and S. Reynaud. Casimir force between partially transmitting mirrors. *J. de Phys. I*, 1:1395, 1991.

- 41 F. Jülicher, A. Ajdari, and J. Prost. Modeling molecular motors. *Rev. Mod. Phys.*, 69:1269, 1997.
- 42 O. Kenneth and I. Klich. Casimir forces in a t-operator approach. *Phys. Rev. B*, 78:014103, 2008.
- 43 O. Kenneth, I. Klich, A. Mann, and M. Revzen. Repulsive casimir forces. *Phys. Rev. Lett.*, 89(033001), 2002.
- 44 D. E. Krause, R. S. Decca, D. López, and E. Fischbach. Experimental investigation of the casimir force beyond the proximity-force approximation. *Phys. Rev. Lett.*, 98:050403, 2007.
- 45 A. Lambrecht, P. A. Maia-Neto, and S. Reynaud. The casimir effect within scattering theory. *New. J. Phys.*, 8:243, 2006.
- 46 S. K. Lamoreaux. Demonstration of the casimir force in the 0.6 to 6 μm range. *Phys. Rev. Lett.*, 78:5, 1997.
- 47 E. M. Lifshitz. The theory of molecular attractive forces between solids. *Sov. Phys. JETP*, 2:73, 1956.
- 48 F. Marchesoni, S. Savel'ev, and F. Nori. Achieving optimal rectification using underdamped rocked ratchets. *Phys. Rev. E*, 73:021102, 2006.
- 49 J. L. Mateos. Chaotic transport and current reversal in deterministic ratchets. *Phys. Rev. Lett.*, 84:258, 2000.
- 50 U. Mohideen and A. Roy. Precision measurement of the casimir force from 0.1 to 0.9 μm . *Phys. Rev. Lett.*, 81:4549, 1998.
- 51 J. N. Munday and F. Capasso. Precision measurement of the casimir-lifshitz force in a fluid. *Phys. Rev. A*, 75:060102, 2007.
- 52 J. N. Munday, F. Capasso, and V. A. Parsegian. Measured long-range repulsive casimir-lifshitz forces. *Nature*, 457:170, 2009.
- 53 P. A. M. Neto, A. Lambrecht, and S. Reynaud. Casimir effect with rough metallic mirrors. *Phys. Rev. A*, 72:012115, 2005.
- 54 P. A. M. Neto, A. Lambrecht, and S. Reynaud. Roughness correction to the casimir force: Beyond the proximity force approximation. *Europhys. Lett.*, 69:924, 2005.
- 55 V. A. Parsegian. *Van der Waals Forces*. Cambridge University Press, Cambridge, England, 2005.
- 56 S. J. Rahi, T. Emig, R. L. Jaffe, and M. Kardar. Casimir forces between cylinders and plates. *Phys. Rev. A*, 78:012104, 2008.
- 57 S. J. Rahi, A. W. Rodriguez, T. Emig, R. L. Jaffe, S. G. Johnson, and M. Kardar. Non-monotonic effects of parallel sidewalls on casimir forces between cylinders. *Phys. Rev. A*, 77:030101, 2008.
- 58 P. Reimann. Brownian motors: noisy transport far from equilibrium. *Phys. Rep.*, 361:57, 2002.
- 59 A. W. Rodriguez, M. Ibanescu, D. Iannuzzi, F. Capasso, J. D. Joannopoulos, and S. G. Johnson. Computation and visualization of casimir forces in arbitrary geometries: Nonmonotonic lateral-wall forces and the failure of proximity-force approximations. *Phys. Rev. Lett.*, 99:080401, 2007.
- 60 A. Roy, C. Y. Lin, and U. Mohideen. Improved precision measurement of the casimir force. *Phys. Rev. D*, 60:111101, 1999.
- 61 A. Roy and U. Mohideen. Demonstration of the nontrivial boundary dependence of the casimir force. *Phys. Rev. Lett.*, 82:4380, 1999.
- 62 D. M. Wood and N. W. Ashcroft. Quantum size effects in the optical properties of small metallic particles. *Phys. Rev. B*, 25:6255, 1982.